Large Eddy Simulation of Flow around a Turbine Blade with Incoming Wakes

V. Michelassi*, J.G. Wissink, J. Fröhlich, W. Rodi
Institut für Hydromechanik, Universität Karlsruhe
Kaiserstrasse 12, 76128 Karlsruhe, Germany

Abstract

The flow around a low-pressure turbine rotor blade with periodically incoming wakes at a realistic Reynolds number is computed by means of LES. The computed results are discussed in terms of phase-averaged and mean quantities. A comparison is made with an existing DNS for the same geometry and operating conditions. Particular attention is devoted to flow structures associated with the incoming wakes, and their effect on the boundary layers. The analysis of the flow field reveals patterns similar to those encountered in DNS and in LES of flow in the same geometry at a lower Reynolds number. Noticeable differences occur in the suction side boundary layer, which exhibits a complete transition to turbulence for the present case.

Nomenclature

b	two-dimensional anisotropy tensor $\overline{b_{ij}} = \overline{u_i u_j} / 2\overline{k} - \frac{1}{3} d_{ij}$
C	chord
C_f	skin friction coefficient = $\tau_{wall} / \left(\frac{1}{2}\rho U_1^2\right)$
C_p	time-averaged static pressure coefficient $= 2\left(\overline{p} - \overline{p_1}\right) / U_1^2$
d	diameter
D	velocity defect $D = \lvert\langle \mathbf{v} \rangle\rvert - \lvert\overline{\mathbf{v}}\rvert$
f	reduced frequency $f = (1/T) \cdot C / U_2$
h	span-wise extent
H	shape factor $= d^*/q$
k	turbulent kinetic energy
l	pitch
n	direction normal to the wall
p	static pressure
P_k	production rate of turbulent kinetic energy

Re	Reynolds number
S	symmetric part of velocity gradient tensor
t	time
T	time period = $l/\lvert u_b \rvert$
U	velocity magnitude
v	velocity vector

Greeks

β	flow angle
δ^*	displacement thickness
Φ	phase
γ	stagger angle
λ	eigenvalue
θ	momentum thickness
τ	shear stress
Ω	anti-symmetric part of velocity gradient tensor

Subscripts and symbols

ax	axial
b	bar
w	wake
1	inlet
2	outlet
$\bar{f}$	time-average of f
$\langle f \rangle$	phase-average of f

1. Introduction

The high complexity of turbomachinery flows, which are three-dimensional (3D), unsteady, and often transitional, requires powerful computational tools and models. In recent years computational methods as well as turbulence modelling based on classical Reynolds averaging could be improved to allow the successful simulation of two-dimensional (2D) [7], quasi 3D [15] and 3D [4] realistic flows in turbine and compressor stages. The target of most of the simulations was the aerodynamics of the stator-rotor interaction and the rotor boundary layer-wake interference

[3]. In a real turbine stage, the unsteadiness and the disturbances convected by wakes generated by the preceding blade row are of great importance because they heavily affect the blade aerodynamic performances. Hence, in view of practical engineering applications, models able to predict the boundary layer state have been developed in the past (see [13]); applications range from very crude algebraic models to complex, and more accurate, models based on transport equations [2, 15]. Still, most of these formulations do not ensure sufficient generality in the presence of impinging wakes. Direct Numerical Simulation (DNS) [25,26] and Large Eddy Simulation (LES) [14,18], are able to provide a much deeper insight in the wake- boundary layer interaction mechanism as compared to 2D unsteady Reynolds Averaged Navier-Stokes (URANS) simulations.

On the experimental side, the effect of incoming wakes on boundary layers was investigated both on flat plates [10] and in linear turbine cascades [11,22,23,24]. The two cases revealed considerable differences in the boundary layer development due to the pressure gradients encountered in the latter flows. Apparently, the strong acceleration in the first 40 to 50% of turbine blades suppresses most of the velocity fluctuations in the wake core so that the boundary layer often stays laminar, or relaminarises [16,26,25] shortly after the leading edge.

Although the DNS of a realistic turbine stage is far beyond the capabilities of modern supercomputers, recent results have shown that both DNS and LES [27,28] allow a detailed examination of the wake transport and the consequent impact on the blade boundary layers. These refined simulations revealed how the vorticity convected by incoming wakes affect the near wall flow [16,25,26]. In particular DNS of the flow around turbine blades with incoming wakes was successfully carried out at Re of 5.18×10^4 [16,25] and 1.48×10^5 [26].

The DNS calculations are extremely costly and the question arises whether similar results cannot also be obtained by LES with considerably lower computational effort. LES calculations of the low Re case (Re=5.81×10^4) are compared with the DNS in [16] and show overall good agreement. Unfortunately, however, this case, in which intermittent separation occurs on the suction side near the trailing edge, is not representative of realistic design conditions. The present paper reports on LES of the flow around a low pressure turbine blade with incoming wakes at a higher, more realistic Re, and the case at Re=1.48×10^5 simulated by Wu and Durbin [26] by DNS was chosen. The results are compared with this DNS and are analysed in detail, with particular focus on the interaction of the wakes with the boundary layers on both pressure and suction side.

2. The geometry and the operating conditions

The geometry is that of the low-pressure aft-loaded turbine blade T106, assembled in a linear test rig [23,24], which was selected by Wu and Durbin[26] for their DNS. Since the blade aspect ratio (h/C) is 1.76, with a blade chord C of 100mm, the flow at mid-span can be considered two-dimensional, thereby allowing 3D simulations to be performed under the assumption of a homogeneous flow in the span-wise direction. The blade stagger angle γ, the inlet angle β_1, and the outlet angle β_2, defined with respect to the axial direction as displayed in Figure 1 are 30.72 deg, 37.7 deg and -63.2 deg, respectively. In the measurements, which were carried out at $Re=5.18\times10^4$ and 2×10^5, the effect of an upstream row of blades was simulated by a moving bar wake generator with a bar diameter to pitch ratio of $d_b/C=0.02$. Unfortunately, the bar-to-blade pitch ratio is not an integer number (0.4/0.525). To yield an exactly periodic flow, the simulations should hence be carried out by using eight blade vanes, which would require an excessive number of grid nodes. Therefore, to reduce the computational effort and still have a reference data set, the operating conditions used in the DNS by Wu and Durbin[26] were selected. In this l/C is 0.799, both the blade and wake pitch are 80mm, and the Reynolds number, based on the axial chord and inlet conditions, is 1.48×10^5 . If computed with the blade chord and exit conditions, as normally done in the turbomachinery field, the Reynolds number is 2.7×10^5.

3. Computational details

3.1 Computational grid and flow solver

The computational domain, displayed in Figure 1, has been chosen to match the one employed in the DNS of Wu and Durbin [26] which extends $0.5\times C_{ax}$ upstream of the leading edge of the blades and $1.0\times C_{ax}$ downstream of the trailing edge. The span-wise width is $h=0.15\times C_{ax}$. The grid was generated by the elliptic method proposed by Hsu and Lee [6], which ensured a nearly orthogonal mesh close to the blade walls with 646×256×64 nodes in the stream-wise, pitch-wise, and span-wise directions, respectively. In a previous DNS Wu and Durbin [26] first tested a coarse grid, with 769×257×129 points, and subsequently a refined one with 1153×385×129 points. The refined DNS grid places 35 to 40 points inside the suction side boundary layer close to the trailing edge [26], while in the present LES this number goes down to 15-20. This reduction was necessary to control the computational effort and, at the same time, to ensure a fair resolution of the incoming wakes vortical structures. Figure 2 illustrates the grid resolution on the suction side, which is the most demanding; the cell sizes in wall units in the x and z direction, Δx^+ and Δz^+, are below 70 and 15-20, respectively. The plot of Δy^+ - which is the distance of the cell centre of the wall-adjacent cell to the wall in wall units - shows values around 3 for $x/C_{ax}<0.55$, while going down to 1 approaching the trailing edge where the boundary layer thickens. These values indicate that the boundary layer is probably not sufficiently resolved for $x/C_{ax}<0.6$-0.7. Along most of the pressure side Δy^+ remains below 1.0. Only near the leading edge it reaches a peak of 2.0 and for $x/C_{ax}>0.8$ it gradually grows until it reaches a value of 5.5 just upstream of the trailing edge.

The simulations have been carried out using the LESOCC [1] code which discretizes the equations for incompressible flow by means of a second-order cell-centred Finite Volume method with centred interpolation of the fluxes. To avoid a decoupling of the velocity field and the pressure field, the momentum interpolation procedure of Rhie and Chow is employed [20]. The implicit solution of the Poisson equation for the pressure correction equation required by the employed SIMPLE method, originally adopted in [1], is complemented with a Fourier solver in the span-wise direction [14] which substantially reduces the computational effort to enforce mass conservation. The equations are solved by marching in time with a three-stage Runge-Kutta algorithm. The mass conservation step was converged to a residual of 10^{-8}. The SGS model used in the LES is the dynamic model by Germano et al. [5] with the modification of Lilly [9]. It employs an eddy viscosity model together with a procedure of reducing the model constant whenever the flow is well resolved. For the present computation, the SGS model employs filtering and averaging in the homogeneous span-wise direction.

3.2 Boundary conditions, phase averaging and computational time

A no-slip boundary condition is enforced at the surface of the blade. The periodicity condition, enforced in the pitch-wise direction, is not critical since the size of the expected flow structures is a small percentage of the blade pitch. In the span-wise direction as well, it is common practice to enforce the periodicity of the instantaneous flow since the dynamically relevant motions have a span-wise extent smaller than the size of the computational domain. The inflow boundary condition for the wakes is enforced by using the database which was kindly made available by Wu and Durbin [27], who generated the incoming wakes with preliminary LES. In the current simulations the wake data closely resembles those adopted in the DNS [26]. The wake half-width is $0.04\times C_{ax}$ combined with a maximum mean wake velocity deficit of 18%. The non-dimensional tangential velocity of the wake is $u_b=-1.204$, and the time period, i.e. one blade-pitch sweep of the wake, is T=0.77239. (Throughout the paper, the inlet velocity U_1 and the axial chord C_{ax} are used as reference quantities.) In order to properly resolve the wake in both space and time, one period T is resolved with 10240 time steps, which corresponds to a non-dimensional time step of $\Delta t=7.543\times10^{-5}$. By adopting this value the CFL number is always below unity. Phase-averaging is performed every 160 time steps to obtain 64 equally spaced phase-averaged snapshots of the flow field, labelled by their phase, $\Phi=0/64$ to 63/64, while t/T is used for instantaneous quantities. Vectors are denoted in bold face. Like in the DNS, the phase-averaging process is initiated after five periods and subsequently performed over 10 periods. All computations were carried out by using 64 processors on the HITACHI SR-8000 vector-parallel computer of the University of Stuttgart with a total computational time of approximately 800 hours.

4. Time averaged pressure distribution around the blade

Figure 3 compares the time-averaged static pressure coefficient, $\bar{C}_p$, around the blade surface with the coarse and refined grid simulations of Wu and Durbin [26]. The flow encounters a strong favourable pressure gradient in the first 60% of the suction side, downstream of which the flow decelerates. On the pressure side the pressure gradient remains substantially flat and close to zero in the first 50% of the blade. Further downstream, the flow experiences a strong acceleration, which persists up to the trailing edge. Such behaviour is typical for mildly loaded low speed turbine rotors. Figure 3 also shows that the static pressure coefficient predicted by the LES is in very good agreement with DNS on the entire pressure side as well as on the suction side up to 80% of the axial chord. For $x/C_{ax}>0.8$ DNS and LES show some differences. Apparently the pressure level predicted by LES is lower than that of DNS; the next sections will prove that this is linked to the boundary layer state. Nevertheless it is interesting to observe that the refined DNS plot deviates from the coarse DNS into the direction of the LES profile. In general, slight differences are located in the region where the flow experiences an adverse pressure gradient (APG) and a thickening of the boundary layer is expected.

5. Wake migration and dynamics

The wake is subject to severe straining inside the vane, as pointed out by Wu and Durbin [26] and, subsequently by Michelassi et al. [16] and Wissink [25] at a lower Re. The flow path of the wake is linked to the principal axes of the time averaged flow field, which correspond to the eigenvectors of the strain-rate tensor and illustrate the direction of compression and stretching, as reported in Figure 4a: the thin arrows identify the direction of stretching, σ_1, while the thick ones identify the direction of compression, σ_2. The magnitude of the vectors is not made proportional to the respective eigenvalues to ease the identification of the vector's direction. The direction and strength of the principal axes does not substantially change in time, as also suggested by Wu and Durbin in their DNS of the same flow.

Figure 4b, in which the wake is traced by the velocity defect vectors $\langle \mathbf{v}_W \rangle = \langle \mathbf{v} \rangle - \bar{\mathbf{v}}$, illustrates the impact of the background flow, in particular of the stretching and compression of the wake. When the wake is aligned with the direction of stretching as in the upper part of the vane, its width decreases as visualised by the two parallel lines labelled “A” in Figure 4b. From the apex to the suction side, the wake is not aligned with either the direction of compression nor that of stretching so that its width remains almost unchanged with respect to the inlet (see the parallel segments labelled “C”). A totally different picture arises at the bow apex of the wake. Here the wake is almost perfectly aligned with the direction of compression so that it widens notably (see the parallel segments labelled “B”). The same figure illustrates the presence of two counter-rotating vortices around the wake which, together with the principal axis pattern, are in excellent qualitative agreement with what discovered in the DNS [26].

Figure 5 shows how the velocity defect D, defined as the difference between the magnitude of the phase averaged velocity vector minus the magnitude of the velocity vector of the time averaged field-can become positive. This phenomenon, already discovered in the DNS by Wu and Durbin [26], can be explained as follows. Suppose the wake being straight and the vector $\langle \mathbf{v}_w \rangle$ vanishing remote from the wake. Then, $\langle \mathbf{v}_w \rangle$ has to be tangential to the wake since otherwise this contradicts continuity normal to the wake. If the wake is deformed this remains qualitatively correct (the momentum exchange initiates $\langle \mathbf{v}_w \rangle$ in the surrounding fluid, small in the beginning and gradually increasing in time) which is visible in Figure 4b. The vector $\langle \mathbf{v}_w \rangle$ changes its orientation so as to remain aligned with the position of the wake. This is clearly visible in Figure 5. Hence, if $\langle \mathbf{v}_w \rangle$ has a component in the opposite direction of the mean flow, as it is the case upstream of the blades and in the lower part of the vane, this yields D<0 as usual (see B at ϕ=4/8). If $\langle \mathbf{v}_w \rangle$ turns into the direction of the mean flow, as it happens in the upper part of the vane, this yields a positive velocity defect, D>0 (see A at ϕ=4/8).

The three-dimensional visualisation of the wake distortion requires to identify the incoming vortical structures. Jeong and Hussain [8] suggested to identify vortices by computing the second largest eigenvalue, λ_2, of $S^2+\Omega^2$. Wu and Durbin [26] found no differences when using either the instantaneous field or when first subtracting the span-wise mean velocity. Therefore λ_2 was computed here using the instantaneous velocity field. Figure 6 shows iso-surfaces of $\lambda_2<0$. The incoming vortical structures are clearly visible and it is possible to follow their dynamics while the wakes travel across the blade vane. The snapshots refer to four instants equally spaced in time over one full period T. Before entering the turbine vane only weak structures are visible, which are primarily oriented parallel to the wake (see t/T=14 in proximity to the leading edge of the upper blade). The DNS [26] showed a more chaotic picture of the incoming vortical structures without any preferred orientation, probably on account of the finer resolution of the grid in the flow core. As in the DNS [26], the LES illustrates how the stretching aligns the vortices along the principal axis σ_1 near the pressure side. Along this direction vorticity is amplified and, while the wake is gradually stretched, it evolves into elongated circular tubes which persist all along the pressure side of the blade. The local structures are elongated, as illustrated by the increasingly large distance between the apex of the wake and the position of its impingement on the pressure side. Together with the progressive alignment of the wake with the direction of stretching, the vortex filaments become more and more distinct. Apparently LES allows capturing the essential features of the wake distortion as already evidenced by DNS: reorientation by convection (t/T=14), and mean straining as the wake is swallowed into the turbine vane (t/T=14+2/8), despite the reduced blade-to-blade grid resolution (165000 nodes against 440000 of the DNS). Figure 6 also illustrates a difference between the lower and upper arms of the wake: the upper one shows regular and well defined structures in proximity to the pressure side, whereas the lower one appears more chaotic and with a slightly superior degree of small-scale motion. In the DNS this difference, located in the region of adverse pressure gradient, was more pronounced. The discrepancy must be attributed to the reduction in the incoming wake resolution provided by the LES grid, since it takes place sufficiently away from the suction side wall.

6. The pressure side

6.1 Flow visualisation and flow structures

In their DNS, Wu and Durbin [20] argued that the pressure side vortices are not Görtler vortices generated by the instability of the pressure side boundary layer, but are flow structures stemming from the incoming vorticity of the wake. They corroborated their conjecture by plotting the λ_2 iso-surfaces in proximity to the pressure side, similar to what is illustrated in Figure 7 for the present LES. The elongated vortices correspond to those of Figure 8 and Figure 9 for two cross-flow sections close to the pressure side located at x/C_{ax}=0.3 and 0.7 respectively. At t/T=14, the incoming vorticity is evidenced by a small vortex core (see the arrow labelled “A”) which is convected and elongated downstream, while it progressively aligns with the pressure side.

In an attempt to verify the accuracy of the LES, this paragraph will repeat the same plots as given by Wu and Durbin [26] in their DNS of the same flow. Figure 8 shows the fluctuating velocity vectors, with the spanwise-averaged mean subtracted, in the plane located at x/C_{ax}=0.3, as illustrated by Figure 7, which extends 6% C_{ax} into the flow core from the pressure side. The eight consecutive instants, covering two time periods as in the DNS, show several counter-rotating vortex pairs in the immediate proximity of the pressure side wall (see for example t/T=15 and 15.25).

Although a direct comparison of instantaneous flow fields is clearly impossible due to their random content witnessed by the differences between two consecutive periods, Figure 8 shows flow patterns quite similar to the DNS. The large rotating structures visible at $t/T=15.50$ and $0.05<x<0.10$, for example, belong to the wake, and they repeat at $t/T=16.5$. These are qualitatively the same macro-structures identified in Figure 7 by "B" at $t/T=14+4/8$, the generation of which was discussed above: the longitudinal vortices turn into counter-rotating vortices near the wall which cause up/down-wash of low/high momentum fluid. The LES identifies weak and small vortices close to the wall, which have an opposite sense of rotation with respect to those of the wake core due to the no-slip condition enforced at the wall already at $t/T=15.50$. The vortical structures are in perfect agreement with the results given in [26]. At $t/T=15.75$, the cross section illustrates how the primary vortex disappears because it has gradually collapsed while approaching the wall, and it generates the two vortex pairs at $z=0.075$ and 0.125. The two vortex pairs are gradually attenuated ($t/T=16.00$ and 16.25) before the next wake crosses the plane at $x/C_{ax}=0.3$ and the process is further iterated in time.

Figure 9 shows the cross-flow plane located at $x/C_{ax}=0.7$ at four instants. This plane is located further downstream, hence the wake arrives somewhat later. The negative fluctuating streamwise velocities produce a mushroom-like contour, as in the DNS, which corresponds to the transport of low-momentum fluid away from the wall promoted by each pair of counter-rotating vortices. This low momentum fluid spreads in the span-wise direction and gives the structures illustrated in Figure 9. As in the DNS, the mushrooms are often asymmetric, with the largest arm corresponding to the strongest of the two originating counter-rotating vortices. The comparison with the fluctuating velocity vectors of the same figure for the same instants reveals a much more complex flow pattern than that encountered at $x/C_{ax}=0.3$. This can be explained by looking again at the λ_2 iso-surfaces of Figure 7. At $x/C_{ax}=0.3$ the pressure side experiences an intermittent growth and decay of the vortex structures. When proceeding further downstream, the wakes, which are identified by the elongated vortices, are already virtually aligned with the blade wall, and are found along the pressure surface for $x/C_{ax}>0.3$-0.4 untill the trailing edge. These structures are permanently present (see again Figure 7). As a result, in this portion of the pressure side the vortex filaments stemming from consecutive wakes overlap and generate a large number of structures. The final picture of the flow is remarkably more complex than that encountered for $x/C_{ax}=0.3$, as illustrated by the fluctuating velocity plot of Figure 9, and it substantially fits with the existing DNS.

6.2 Time- and phase-averaged profiles

Figure 10 illustrates the status of the pressure side boundary layer. For $x/C_{ax}>0.1$ the skin friction coefficient, $\overline{C}_f$, grows due to the flow acceleration which is mild in the first 60% of the blade, and quite strong further downstream. The values of $\overline{C}_f$ are always in the range of laminar or early transitional boundary layer over a flat plate [19]. The boundary layer edge, needed for the computation of boundary layer integral parameters and $\overline{H}$, is determined by a procedure based on the local vorticity (see Michelassi et al., [15]). The shape factor experiences a sudden increase up to the value of 3 in proximity to the stagnation point where the pressure gradient is first strongly adverse, and then almost zero (see also Figure 3). Further downstream, up to $x/C_{ax}<0.6$, $\overline{H}$ gradually reduces down to 1.8-2.0 due to the effect of the impinging wakes, and then it slightly raises again while levelling off at a value of 2.3 in the strongly favourable pressure gradient region. Apparently the time averaged boundary layer is never truly turbulent as $\overline{H}$ never drops below 1.8-2.0, despite the strong and intermittent disturbances discussed in the previous section.

The time averaged behaviour of the flow on the pressure side may be better understood with the help of Figure 11 which reports the phase-averaged shape factor, $\langle H \rangle$, and the momentum thickness, $\langle q \rangle$, for six sections normal to the pressure side-wall located at 20-40-50-60-70-80% of the axial chord. The boundary layer has a strongly intermittent nature only in the first 60% of the axial chord, as proved by the up-down shape of the curves. Then, both the shape factor and the momentum thickness are nearly constant for $x/C_{ax}>0.6$. Apparently, there is a mild increase of momentum transfer in the boundary layer due to the intermittent presence of the impinging wakes, causing some change of the velocity profile towards a turbulent boundary layer. Nevertheless, both the time averaged and phase averaged H values suggest that transition does not really take place. The three sections at $x/C_{ax}=0.4$-0.5-0.6 periodically become almost turbulent ($\langle H \rangle \cong 1.6$), but they relaminarise when the wake is far from the pressure side wall. The two sections further downstream ($x/C_{ax}=0.7$, 0.8) show almost constant values for both quantities: the static pressure coefficient (see Figure 3) indicates that the nearly constant-in-time nature of the boundary layer is due to the concerted action of the favourable pressure gradient and the overlap of several wakes for $x/C_{ax}>0.6$ which masks the effect of each single incoming wake, as suggested by the λ_2 isoline plot of Figure 7. At 60% of the axial chord the shape factor reaches its lowest value: for this reason both the phase-averaged turbulent kinetic energy and production rate are shown at this section in Figure 12 . Close to the pressure-side wall, for $n/C_{ax}<0.02$ and for all phases, there is always a core with relatively large values of $\langle k \rangle$ and $\langle P_k \rangle$. Both are very moderately boosted by the impinging wakes (the position of which is shown by the black arrows for the first phase). The situation does not change in the other five cross sections, and the same happens when plotting the phase averaged components of the Reynolds stress tensor.

To understand why the boundary layer remains substantially laminar despite the peak of k, Figure 13, 14, and 15 show respectively the wall normal profiles of the time averaged velocity, $\overline{u}$, the turbulent kinetic energy, $\overline{k}$, and the normal stresses in the streamwise, $\overline{uu}$, normal, $\overline{vv}$, and spanwise, $\overline{ww}$, directions at the same six axial locations (20-40-50-60-70-80% C_{ax}) of Figure 11. The DNS data [26] are also inserted for comparison. The time averaged velocity profiles of Figure 13 show that in the first two sections (20-40% C_{ax}) the boundary layer is quite thick on account of the nearly zero pressure gradient. It then narrows further downstream due to the strongly favourable pressure gradient encountered for $x/C_{ax}>0.6$, the effect of which is visible in the $\overline{C_f}$ plot of Figure 10. The good agreement with the profiles computed by Wu and Durbin [26] suggests that the velocity field predicted by the LES is fairly close to that given by the DNS. Figure 14 performs a more challenging comparison by displaying profiles of the time averaged turbulent kinetic energy at the same six sections. The profiles computed by the present LES report the resolved velocity fluctuations only without the SGS-contribution. The turbulent kinetic energy peak as predicted by both DNS and LES constantly grows while proceeding towards the trailing edge. Still, if the turbulent kinetic energy peak is made non-dimensional with respect to the local velocity, $\overline{k}/u_{loc}^2$, the ratio decreases, as shown in Figure 16 with the exception of the first 40% of the blade. This suggests that the local turbulence intensity indeed decreases while approaching the trailing edge under the overwhelming effect of the favourable pressure gradient, and the boundary layer stays laminar. Except for the first section, the kinetic energy in the LES matches the DNS data fairly well (see in particular the peak located at $n/C_{ax}\approx0.004C_{ax}$). The reasons for missing the shoulder at $0.01<n/C_{ax}<0.02$ are not totally clear, but stem probably from the reduced grid resolution in the flow core where part of the contribution to k transported by the wake and resolved in the DNS is lost in the LES. Figure 15 shows the three normal stresses and compares the spanwise component with the DNS. The various components are scaled differently to enhance visibility of the spanwise and normal stresses with respect to the streamwise component. The spanwise component compares favourably with the DNS, with the exception of the first section. The plots reveal that the streamwise component is approximately 5 times larger than the other two for each of the six sections, which is again in agreement with the DNS, reported at one station ($x/C_{ax}=0.30$). Hence, down to the trailing edge, the fluctuations are very anisotropic and the overwhelming contribution to the peaks of $\langle k \rangle$ visible in Figure 12 stem from the streamwise velocity fluctuations such that truly three-dimensional turbulence does not prevail. In fact, the fluctuations observed in the boundary layer correspond to the longitudinal vortices shown in Figure 7, which are nothing else than the footprints of impinging wakes. Wu and Durbin [26] suggest that these vortices promote the up/down-wash of low/high momentum in the boundary layer. The large difference in magnitude between streamwise fluctuations and normal and spanwise fluctuations, respectively, can be explained by the findings that the straining of plane wakes by the free-stream velocity can promote unidirectional fluctuations to become an order of magnitude larger than fluctuations in other directions (Rogers [21]). The lack of fully three-dimensional turbulent activity is also confirmed by the relatively weak correlation between u and v fluctuations as witnessed by the structural parameter $\overline{uv}/k$. At x/C_{ax}=0.6, where the time-averaged shape factor is minimum, this ratio has always values about half the size of those observed in a fully turbulent boundary layer (i.e. at y^+~10-12 a value of 0.058 is obtained instead of 0.10-0.12). This is the reason why the boundary layer never develops full turbulence, despite some sudden drop of the shape factor at around x/C_{ax}=0.6. Further downstream the relative magnitude of the various components does not change, because the strong favourable pressure gradient inhibits the growth of the disturbances introduced by the wakes.

7. The suction side

In this section we discuss the transition scenario on the suction side as described by the present LES and perform some comparison with the DNS of Wu and Durbin [26] in order to investigate the impact of the LES modelling on the transition. The DNS reveals a relatively complex scenario. The presence of the impinging wakes causes transition near the leading edge. Past transition, there is a region which remains turbulent at all times due to the strong adverse pressure gradient, visible in Figure 3, and the way the wakes wrap around the nose of the blade. Due to the favourable pressure gradient further downstream, the flow subsequently relaminarizes. Beyond x/C_{ax} ~ 0.6, the boundary layer again experiences an adverse pressure gradient inducing deceleration. In the presence of impinging wakes, Wu and Durbin found evidence of by-pass transition with turbulent spots appearing near mid-chord which grow and merge into the fully turbulent trailing edge region. The differences between this by-pass transition scenario and the case without wakes are discussed in [26]. In Figure 17, the skin friction $\overline{C_f}$ along the suction side obtained with the LES is compared with the DNS result. The decrease of $\overline{C_f}$, starting just upstream of x/C_{ax} ~ 0.6, corresponds to the pressure gradient changing from favourable to adverse (see also Figure 3). For $x/C_{ax} < 0.75$, both curves are in good agreement. Downstream of this point, however, the DNS curve starts to increase at $x/C_{ax} = 0.78$ whereas for the LES this takes place later, at x/C_{ax}

= 0.87. Since this increase is directly related to the transition of the boundary layer, we conclude that in the LES transition is delayed by about $0.1C_{ax}$ compared to the DNS.

In order to assess the behaviour of the present LES, isoline-plots of the v velocity component were generated which are equivalent to Figure 8 in [26]. They are reported in Figure 18 for instants corresponding to the four different phases considered here. The back plane serves to identify the instantaneous position of the wake. As expected from a LES, the fluctuations in the v velocity contours are smaller than those obtained in the DNS. Near the leading edge, the effect of the wakes is much smaller. Between t/T=15.50 and t/T=15.75, for instance, the wake introduces small disturbances, but these are not able to trigger real turbulence. Instead, their “lifetime” is so short that one quarter of a period later, they are almost completely damped out. A proper description of the leading edge transition by LES is thought not to be important since the favourable pressure gradient further downstream will damp out the generated fluctuations anyway. Downstream of x/C_{ax} = 0.6, the pressure gradient becomes adverse again. While in the area where the pressure gradient is favourable the impinging wake hardly affects the v velocity inside the boundary layer, downstream of x/C_{ax} = 0.6 the effect of the impinging disturbances on the v velocity is clearly visible (see the graph at t/T=15.00). Hence, contrary to the skin-friction plot suggesting that there are no major differences between LES and DNS for $x/C_{ax} < 0.8$, the v velocity contours tell a different story. The perturbations observed in the region $0.6 < x/C_{ax} < 0.8$ are far too smooth to correspond to turbulent spots. Since the results of [26] show that the turbulent spots are triggered by the impinging wakes, two different causes may be responsible for their suppression in the LES. It is possible that the resolution of the suction side boundary layer in the LES is too coarse to represent sufficient fine-scale fluctuations, resulting in the damping of otherwise unstable modes by eddy viscosity. Furthermore, the wake might be damped excessively on its way from the inlet until it impinges onto the blade. This could be a consequence of the relatively coarse mesh used in the core region (a similar phenomenon is observed on the pressure side where the “knee” in the $\overline{k}$ profiles of Figure 14 is lost due to the grid resolution of the impinging wakes). Values of the eddy viscosity inside the wakes reach up to five times the molecular viscosity thereby damping the small scale wake fluctuations. The trailing edge region is fully turbulent in both DNS and LES. In the LES, however, this region is found to be smaller than in the DNS, due to the late transition in the LES already observed in Figure 17.

Phase-averaged data are presented next. Figure 19 shows wall-normal profiles of the tangential velocity, the spanwise fluctuations $\langle w'w' \rangle$, and the fluctuating kinetic energy $\langle k \rangle$ at x/C_{ax} = 0.8 and x/C_{ax} = 0.9, respectively. Before transition, the difference between the velocity profiles at various phases is almost negligible, reflecting a relatively small influence of the wakes on this quantity. In Figure 19 it is shown that, compared to the fluctuating kinetic energy, at x/C_{ax} = 0.8 the spanwise fluctuations are negligibly small for all phases. Hence, the fluctuating kinetic energy results almost entirely from two-dimensional fluctuations. At x/C_{ax} = 0.9 the situation has changed in that three-dimensional fluctuations are now present, particularly close to the wall. The fluctuating kinetic energy as well as the shear stress (of similar shape as $\langle k \rangle$, but not displayed here) have their maxima at a larger distance from the wall than before. Also the velocity profiles exhibit more variation from one phase to the other in response to the wakes. The profiles of the spanwise turbulent fluctuations $\langle w'w' \rangle$ plotted in Figure 19 show that in the LES the fluctuations in the suction-side boundary layer change over from two-dimensional to three-dimensional in the range $0.8<x/C_{ax}<0.9$. At $\phi=2/8$, a peak in the spanwise fluctuations is obtained very close to the wall in at x/C_{ax}=0.9. According to Figure 18 (t/T=15.25), at this phase the wake impinges somewhat upstream of the trailing edge. For larger ϕ, Figure 19 for x/C_{ax}=0.9 shows a gradual spreading of the spanwise fluctuations away from the wall. At the same time, the spanwise fluctuations close to the wall become smaller. The fact that at $\phi=2/8$ the impingement of the wake near x/C_{ax}=0.9 coincides with a maximum in the spanwise fluctuations, indicates that the production of turbulence near the wall is triggered by the wake.

As discussed above, the boundary layer remains virtually laminar despite the incoming wakes for roughly the first 80% of the blade axial chord. An analysis of what happens close to the trailing edge reveals some interesting features. This analysis is performed with the aid of the phase-averaged shape factor, $\langle H \rangle$, plotted in Figure 20 for 4 sections at 75, 85, 95, and 99% of the blade axial chord. At $x/C_{ax}=0.75$ the position of the wake is located directly to the right of the maximum of $\langle H \rangle$. Its effect on the shape factor is significant, although $\langle H \rangle$ never manages to drop below the value of 2. This suggests that the boundary layer remains basically laminar at all times. When moving further downstream, at $x/C_{ax}=0.85$ the effect of the wake is found to be amplified. This is due to the persistence of a moderate adverse pressure gradient. At x/C_{ax}=95%, the shape factor is constantly below two, indicating a definite presence of turbulence. Shortly after the wake has passed, $\langle H \rangle$ drops to *1.5,* a value typical for turbulent boundary layers. Right at the trailing edge, at $x/C_{ax}=0.99$, the transition is complete since the shape factor is constantly below 1.7.

We proceed analysing the transition scenario using so-called x-Φ space-time plots of the phase-averaged fluctuating kinetic energy at various distances from the wall. The monitoring surfaces are identical with grid planes j=2,6,19,62 as displayed in Figure 21 and follow the surface of the blade. They are located at the first grid node adjacent to the wall (surface 2), inside the boundary layer (surface 6), beyond but still close to the boundary layer (surface 19), and in the free-stream (surface 62). Figure 21 shows their non-dimensional distance from the wall (computed by using the friction velocity of the time averaged flow field). Their wall-normal distance (measured at the crown of the blade, x=0.35) is n/C_{ax} = 0.0008, 0.004, 0.016, 0.073, respectively, which allows to draw a relation to the plots in Figure 19 where the corresponding levels are marked with arrows (except 2). Along these monitoring surfaces the phase-averaged fluctuating kinetic energy was computed using the 64 phase-averaged flow fields and is displayed in Figure 22. To improve visibility, the levels shown are not the same in all figures. The thick white line labelled "w" has been introduced as a reference line for comparison between the pictures and corresponds to the position of the wake at the edge of the boundary layer. This position as a function of time has been determined assuming that the wake is passively convected by the free-stream (as supported by the results of the DNS of Wu and Durbin [26]). For this the inverse of the mean axial velocity at the edge of the suction side boundary layer was integrated in the axial direction in order to determine the path of the wake in axial coordinates. The left-most picture in Figure 22 illustrates that on the surface 2, closest to the suction side boundary, there always exists a portion of flow which shows some turbulence activity, namely from x/C_{ax}˜0.85 until the trailing edge. This corresponds with the transition discussed above with respect to the time-averaged flow (Figure 17). Note that the impinging wake only weakly triggers transition along this surface. For surface 6, shown in the second picture, the influence of the impinging wake on the location of transition is much more pronounced. Each time the wake impinges, the location of transition moves upstream from x/C_{ax}˜ 0.85 to x/C_{ax}˜ 0.65. The coincidence of the impinging wake with the onset of transition is illustrated by the solid black circle which shows that the increase in the fluctuations is clearly aligned with the wake path. As already noted above, Figure 19 clearly shows that these fluctuations are effectively two-dimensional, only further downstream, for x/C_{ax}=0.85, spanwise fluctuations become more important. We can summarise that in the LES transition appears to take place via amplification of 2D modes followed, further downstream, by the amplification of 3D modes which are triggered by the impinging wakes (as observed in Figure 19 for x/C_{ax}=0.9). The periodic pattern of the plot suggests that the wake is responsible for the increase of the fluctuating kinetic energy starting shortly after x/C_{ax}=0.5. From this point onwards, the space-time plot shows the same pattern as identified by Schulte and Hodson [22] who measured the wake-induced transitional flow for a similar turbine blade, labelled "blade H", with a pitch-to-chord ratio of 0.78 and Re=1.3×10^5 based on chord and exit conditions (observe that the Reynolds number based on the axial chord and inlet conditions is approximately 5.6×10^4, against the value 1.48×10^5 of the present simulation). They suggest the presence of a turbulent region clearly triggered by the incoming wakes. In our LES we obtain a region of transitional flow in the triangular shaped portion of the suction side boundary layer labelled "a" (see Figure 22, surface 6). Once the effect of the wake is damped out, the measurements suggested the presence of a so called "becalmed" region in which turbulence is substantially absent. This coincides with the dark region, labelled "b" in Figure 22, that separates the two lighter regions. It is interesting to observe that the becalmed region survives until the next wake passes, but it never reaches the trailing edge of the blade where the boundary layer remains turbulent all the times. Surface 19 is located near the edge of the boundary layer. Therefore, the mean axial velocity at this surface is comparable to the mean axial velocity at the edge of the boundary layer, for this reason the path of the wake coincides with the axis of the "tongue" of fluctuating kinetic energy starting at $x/C_{ax}\tilde{}0.15$, $\phi\tilde{}0.55$. This illustrates that it is possible to use the fluctuating kinetic energy to identify the path of the wake. Note that the level of $\langle k \rangle$ is an order of magnitude lower at this distance, though (see also Figure 19). Surface 62 is located in the free-stream. Here, the levels of fluctuating kinetic energy reached inside the wake are much higher than the levels observed at surface 19. This is a direct consequence of the kinetic energy production inside the bow apex of the wake inside the free-stream and core region of the flow. The detailed study of this mechanism is the subject of a companion paper [17]. Like for surface 19, again the fluctuating kinetic energy identifies the path of the wake as it crosses the surface, which for surface 62 clearly differs from the path of the wake as it impinges on the edge of the boundary layer. This phase lag results from the U-shape of the wake shown in Figure 6 and the back planes in Figure 18 above [26]. The wake advances faster in the core of the flow and is slower at the blade. Hence the wake at surface 62 is ahead of the white line "w" since the latter is related to the position of the wake closer to the surface. On the contrary, the wake lags behind this line for surfaces 2 and 6 in the left two pictures of Figure 22.

An important result of the plots in Figure 22 is the fact that the wakes do not interact with one another. Hence the results can be compared to cases with wakes having a different, in particular lower, frequency. The reason for this weak interaction probably also stems from the relatively small wake strength (half-width=0.04×C, maximum wake velocity deficit=18%), which is directly proportional to the disturbance convected downstream. An often employed quantity to characterise the wake-wake interaction is the so-called reduced frequency, *f*, which compares the incoming wake period with the approximate time the wake takes to travel inside the vane, C/U_2. While in the measurements of "blade H" [22] the reduced frequency is $f = 0.38 - 0.78$, it is $f = 1.08$ in the present investigation, which is only marginally larger. Figure 22 shows that also for this reduced frequency the wakes are far enough apart to avoid wake-wake interaction inside the turbine cascade passage. This means that the results presented here can be compared to other experiments or numerical simulations, having similar geometry and Reynolds number, which also exhibit negligible wake-wake interaction.

8. The flow downstream of the trailing edge

The flow downstream of the trailing edge is of importance because it gives a measure of the unsteadiness which survives from the incoming wakes and is transmitted to the next blade row. Since the inter-row gap is generally in the range of 0.3-0.5×C_{ax}, Figure 23 shows the velocity magnitude, $\langle |U| \rangle$, the flow angle, β_2, and the turbulent kinetic energy at a section located 0.4×C_{ax} downstream of the trailing edge. The lower plots show the time-average profiles along the pitch, while the space-time plots illustrate the fluctuations, triggered by the incoming wakes, of the phase-averaged quantities with respect to the time averaged value. The time-averaged velocity magnitude has changes of approximately 10% of the mean in the pitch-wise direction. The same figure illustrates the positive-negative fluctuations in time due to the wakes; a positive/negative velocity defect (see Figure 5) is responsible for the local increase/decrease of $\langle |U| \rangle$. This fluctuation is of the order of ±3% of the local time-averaged velocity against the value of 18% imposed at the inlet. The average flow angle is slightly larger than what was expected (63.6-deg against the design value of 63.2). The unsteadiness induced by the incoming wakes is at most 2-deg. The plot of the turbulent kinetic energy reveals that the local phase-averaged fluctuations can be 10 times as large as the local time-averaged value. This large scatter is located on the suction side portion of the wake generated by the blade. In general, Figure 23 reveals that the influence of the incoming wake is still visible 40%C_{ax} downstream of the trailing edge. Although both flow velocity and angle are only slightly affected, the turbulent kinetic energy fluctuation peak is quite large. Thereby, the potential effect on the boundary layer of the next blade row is equally large.

9. Conclusions

The LES of the flow in a low speed turbine cascade in the presence of incoming periodic wakes was first compared with an existing DNS. As was to be expected, the flow structures captured by the LES show less detail. Nevertheless, with 5.3 times fewer grid nodes, the present LES provided an overall picture and general flow pattern which agrees fairly well with that of the DNS [26], as evidenced by the flow visualisations.

The analysis of the flow revealed that the complex mechanism which triggers the transition to turbulence of the suction side boundary layer is not fully reproduced. LES predicts a transition point which is delayed by approximately 10% C_{ax} compared to DNS. The analysis of the results indicated that the resolution of the suction side boundary layer is probably not sufficient to describe the fine scale fluctuations and the turbulent spots. Moreover, some of the difficulties in reproducing the skin friction predicted by DNS may partly result from the SGS model and partly from the relatively (with respect to DNS) coarse grid in the flow core, which does not allow to resolve all the fine scale activity convected by the wake. The phase-averaged plots showed interesting similarities with what was discovered during the experimental investigation of the flow in a similar low speed turbine: the periodic appearance of turbulent and becalmed regions on the suction side of the blade was clearly triggered by the wake. A time delay between the onset of turbulence activity in the boundary layer and the position of the wake was also observed. Moreover, turbulence is shown to develop a fully 3D state considerably after the first appearance of stream-wise velocity fluctuations.

On the pressure side there is much closer agreement with the DNS. This is probably due to the reduced effect of the impinging wakes and due to the largely laminar nature of the boundary layer. In fact, the analysis of the simulation revealed that the longitudinal vortices on the pressure side, the interaction with the wall of which promotes pairs of counter-rotating vortices, are potentially able to trigger transition. Nevertheless, due to the strong favourable pressure gradient the strong streamwise velocity fluctuations associated with the longitudinal vortices never manage to promote sufficient levels of spanwise and normal stresses. Hence, the resolved turbulent stresses exhibits quite large anisotropy and the flow never develops fully three dimensional turbulence.

The analysis of the exit flow shows that the effect of the incoming periodic wakes is quite evident, especially in the phase-averaged turbulent kinetic energy, which exhibits fluctuations that are one order of magnitude larger than the corresponding time-averaged value.

The results allow to conclude that the flow pattern provided by the LES is, at least in the present case, sufficiently similar to that predicted by the DNS. In this view, LES can provide data for further RANS model development, with the exception of the transitional portion of the suction side boundary layer where better resolution is necessary. Overall, the computational effort is considerably reduced with respect to DNS. Therefore LES can be expected to play an increasing role in solving flow problems of industrial relevance.

10. Acknowledgements

The authors wish to gratefully acknowledge P.A. Durbin and X. Wu for providing the incoming wake data and the steering committee of the computer centre of the University of Stuttgart for the computing time. This research was funded by the German Research Foundation (DFG) project “Periodic Unsteady Flow in Turbo-machinery”. J. Fröhlich was funded by the DFG-CNRS programme ‘Numerical Flow Simulation’.

11. References

1. Breuer, M., Rodi, W., “Large eddy simulation for complex turbulent flows of practical interest”, Flow Simulation with High Performance Computers II, Notes on Num. Fluid Mechanics, Wieweg Verlag, 1996.
2. Cho, N.-H., Liu, X., Rodi, W., Shönung, “Calculation of Wake-Induced Unsteady Flow in a Turbine Cascade”, ASME Paper 92-GT-306.
3. Dénos, R., T. Arts, G. Paniagua, V. Michelassi, F. Martelli, “ Investigation of the Unsteady Rotor Aerodynamics in a Transonic Turbine stage”, Journal of Turbomachinery, January 2001, Volume 123, Issue 1 pp. 81-89.
4. Emunds, R., Jennions, I.K., Bohn, D., Gier, J. (1999), The Computation of Adjacent Blade-Row Effects in a 1.5-Stage Axial Flow Turbine, ASME Journal of Turbomachinery, 121, 1-10.
5. Germano, M., Piomelli, U., Moin, P., Cabot, W.H., “A dynamic subgrid-scale eddy viscosity model”, Physics of Fluids A 3, number 7, 1991, pp.1760-1765.
6. Hsu, K., Lee, L., 1991, “A numerical technique for two-dimensional grid generation with grid control at all of the boundaries”, J. Comput. Phys., 96, 451-469.
7. Hummel, F., “Wake-Wake Interaction and its Potential for Clocking in a Transonic High-Pressure Turbine”, ASME J. of Turbomachinery, January 2002, vol. 124, pp. 69-76.
8. Jeong, J., Hussain, F., 1995, “On the identification of a vortex”, J. Fluid Mech. 285, 69-94.
9. Lilly, D.K., “ A proposed modification of the Germano subgrid-scale closure method”, Phys. Fluids A4 (3) 633-635, 1992.
10. Liu, X., Rodi, W., “Experiments on transitional boundary layers with wake-induced unsteadiness”, J. Fluid Mechanics. (1991), vol. 231, pp. 229-256.
11. Liu, X., Rodi, W., “Velocity Measurements of Wake-Induced Unsteady Flow in a Linear Turbine Cascade”, Experiments in Fluids, 17, 1994, pp. 45-48.
12. Lumley, J. L., “Computational Modelling of Turbulent Flows”, Adv. Appl. Mech., n. 18, 1978, pp. 123-176.
13. Mayle, R.E., “The Role of Laminar-Turbulent Transition in Gas Turbine Engines”, ASME Paper 91-GT-261.
14. Mellen, C.P., Fröhlich, J., Rodi, W., “Lessons from the European LESFOIL project on LES of Flow around an Airfoil”, AIAA 2002-011.

15. Michelassi, V., Martelli, F., Dénos, T. Arts, C.H. Sieverding, “Unsteady Heat Transfer in Stator-Rotor Interaction by Two Equation Turbulence Model”, Transaction of the ASME – Journal of Turbomachinery, Vol. 121, July 1999, pp. 436-447.
16. Michelassi, V., Wissink, J., Rodi, W., “Analysis of DNS and LES of a Low-Pressure Turbine Blade with Incoming Wakes and Comparison with Experiments”, 2002, Report. N. 789, Institute for Hydromechanics, University of Karlsruhe, Germany.
17. Michelassi, V., Wissink, J., “Turbulent kinetic energy production in the vane of a LP linear turbine cascade with incoming wakes”, to be submitted.
18. Moin, P., “Advances in Large Eddy Simulation Methodology for Complex Flows”, Proceedings, 2nd TSFP, 2001, vol. 1.
19. Pope, S. B., “Turbulent flows”, Cambridge University Press, 2001.
20. Rhie, C.M., Chow, W.L., “Numerical Study of the Turbulent Flow Past an Airfoil with Trailing Edge Separation”, AIAA J., 1983, vol. 21, pp. 1525-1532.
21. Rogers, M.M., “The evolution of strained turbulent plane wakes”, J. Fluid Mechanics. (2002), vol. 463, pp. 53-120.
22. Schulte, W., Hodson, H.P., “Unsteady Wake-Induced Boundary Layer Transition in High Lift LP Turbines”, ASME Journal of Turbomachinery, Vol. 120, January 1998, pp.28-35.
23. Stadtmüller, P., “Investigation of Wake-Induced Transition on the LP turbine Cascade T106A-EIZ”, DFG-Verbundproject Fo 136/11, Version 1.1, 2001.
24. Stadtmüller, P., Fottner, L., “A Test Case for the Numerical Investigation of Wake Passing Effects of a Highly Loaded LP turbine Cascade Blade, ASME Paper 2001-GT-311.
25. Wissink, J.G., “DNS of a separating low Reynolds number flow in a turbine cascade with incoming wakes”, in: Proceedings V International Symposium on Engineering Turbulence Modelling and Measurements, Mallorca (Spain), 16-18 September 2002.
26. Wu, X., Durbin, P.A., “Evidence of longitudinal vortices evolved from distorted wakes in a turbine passage”. Journal of Fluid Mechanics, (2001), vol.446, pp.199-228.
27. Wu, X., Jacobs, R.G., Hunt, J.C.R., Durbin, P.A., “Simulation of boundary layer transition induced by periodically passing wakes”, J. Fluid Mechanics. (1999), vol. 398, pp. 109-153.
28. Xiaoli Huai, Joslyn, R.D., Piomelli, U., “Large Eddy Simulation of Transition to Turbulence in Boundary Layers”, Theoret. Comput. Fluid Dynamics, 1997, n. 9, 149-163.

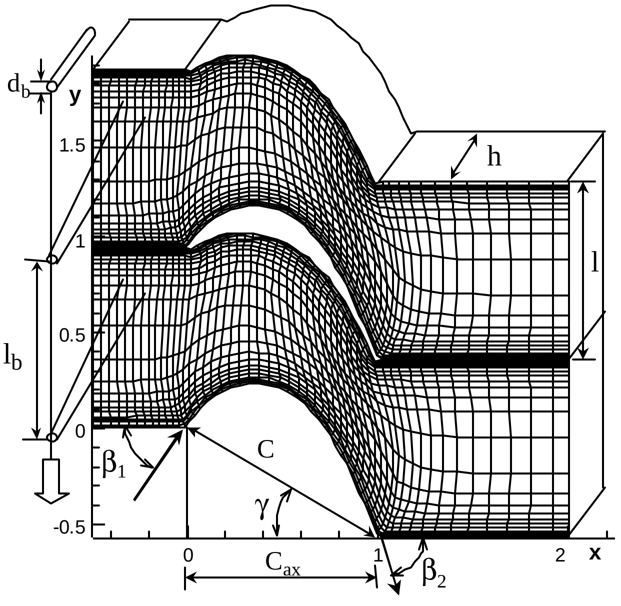

Figure 1. Cascade geometry and grid used for LES (one out of 12 nodes is shown in both stream-wise and pitch-wise directions)

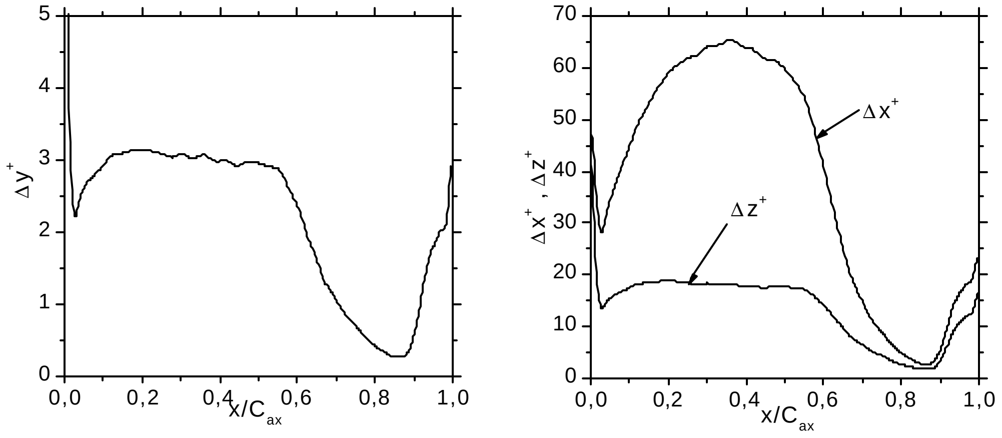

Figure 2. Distance between points in wall units at the blade suction side. Left: distance of wall-adjacent point to the surface, right: wall-parallel point-to-point distances.

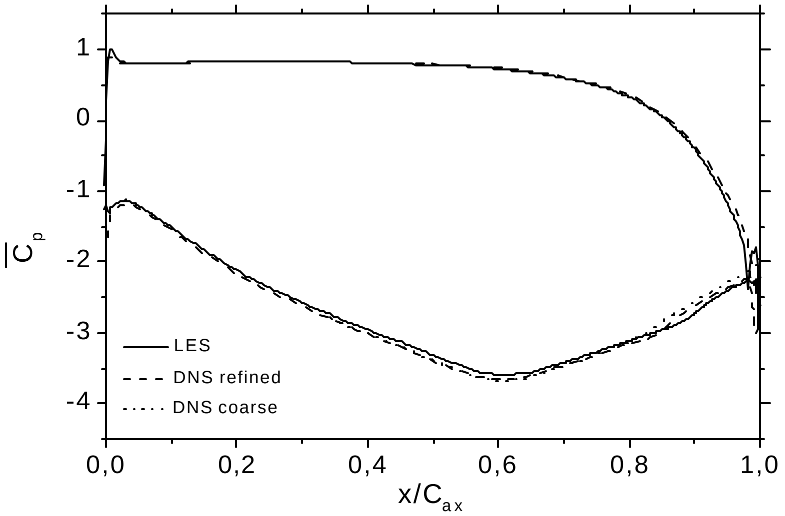

Figure 3. Time-averaged static pressure distribution around the blade.

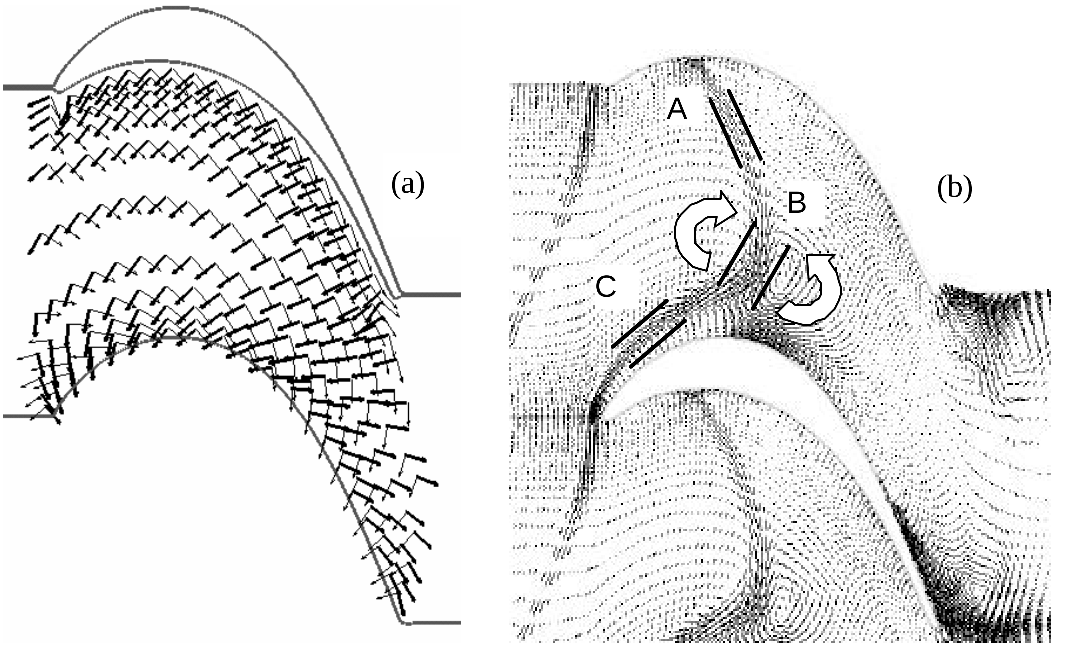

Figure 4. Principal axes of the time-averaged strain-rate tensor $\overline{S_{ij}}$, left (the thick vector identifies the direction of compression, the thin one that of stretching), and wake velocity $\langle \mathbf{v}_w \rangle = \langle \mathbf{v} \rangle - \overline{\mathbf{v}}$ at Φ=3/8, right (twin-thick parallel segments indicate the approximate width of the wake).

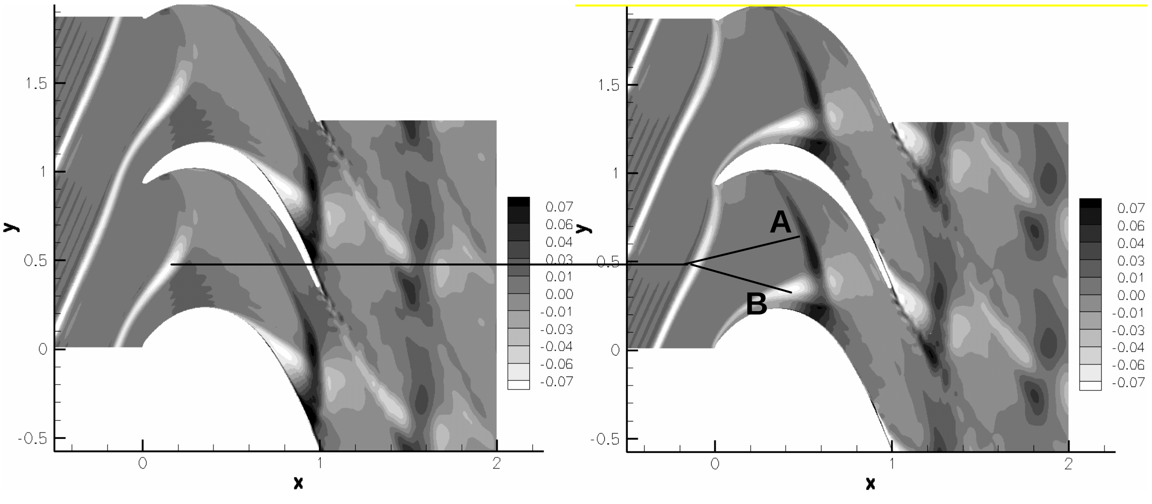

Figure 5. Phase-averaged velocity defect D at ϕ=0/8, 4/8, from left to right.

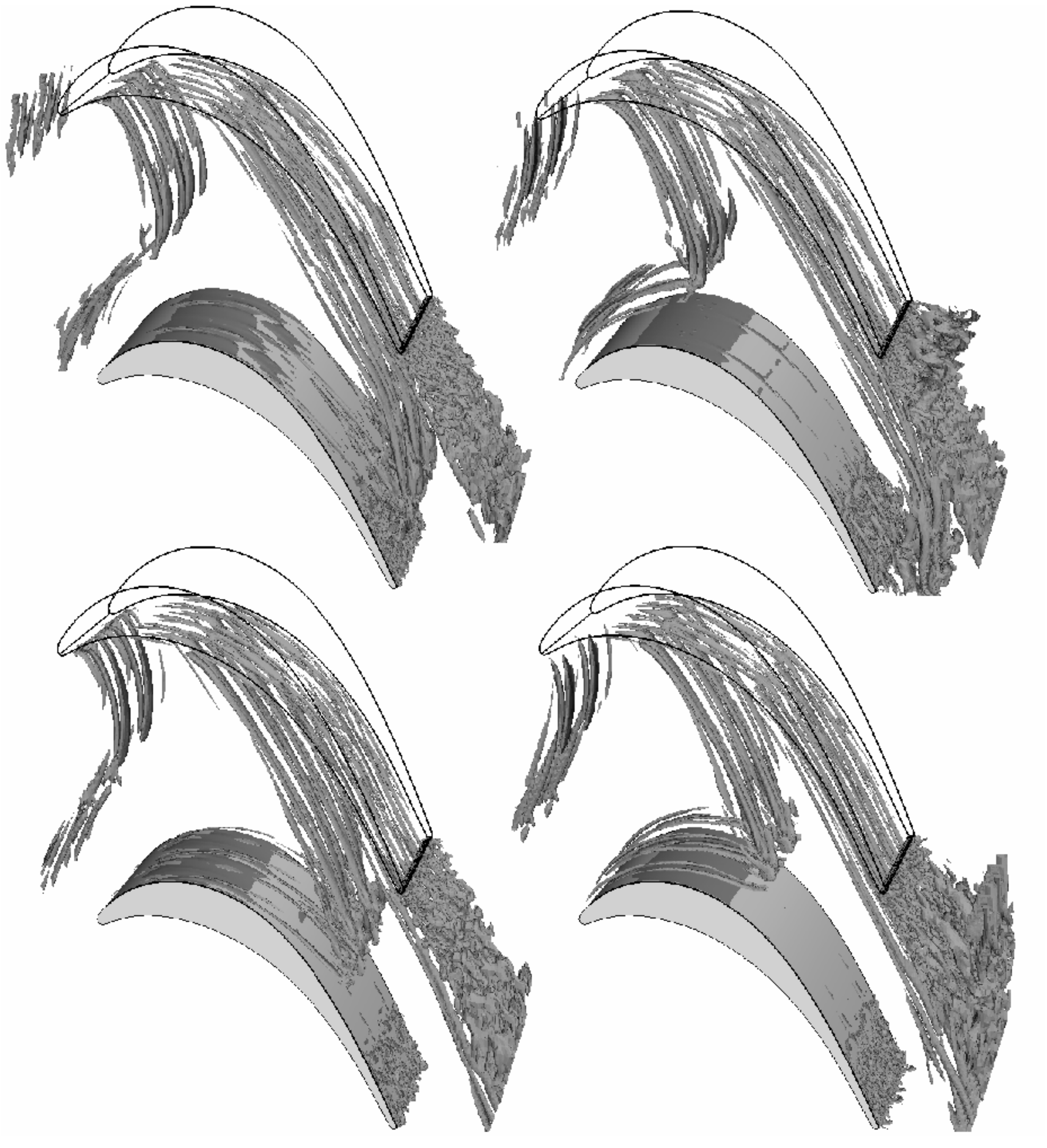

Figure 6. Instantaneous iso-surfaces of λ_2 in the blade vane for four selected times: t/T=14+0/8, 14+2/8, 14+4/8, 14+6/8 from top left clockwise.

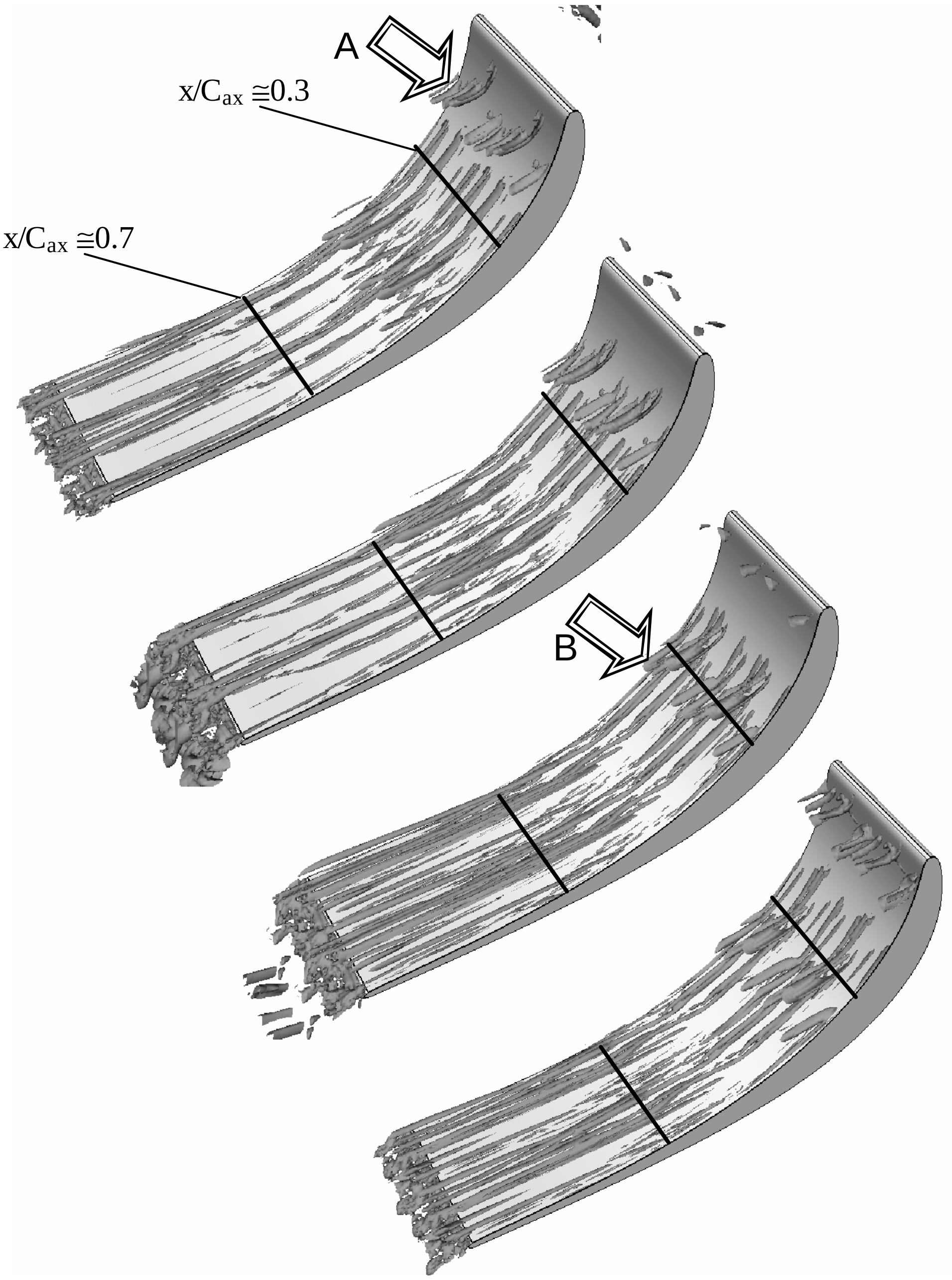

Figure 7. Instantaneous iso-surfaces of λ_2 in proximity to the pressure side for four selected times t/T=14+0/8, 14+2/8, 14+4/8, 14+6/8 from top to bottom.

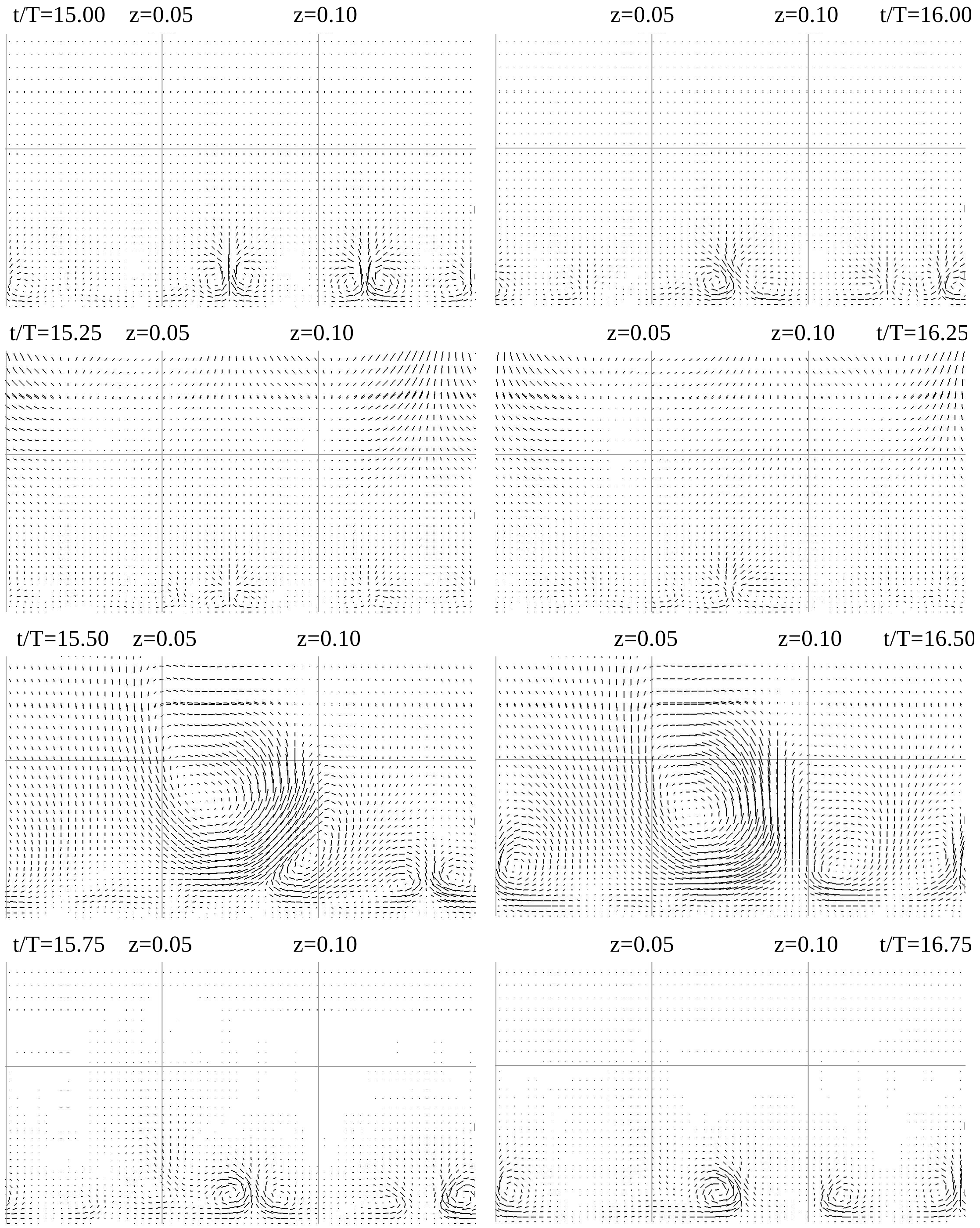

Figure 8. Fluctuating velocity vectors (spanwise-averaged mean subtracted) in the plane perpendicular to the pressure surface, x/C_{ax}=0.3, at eight consecutive instants t/T=15 to 16.75, step=0.25.

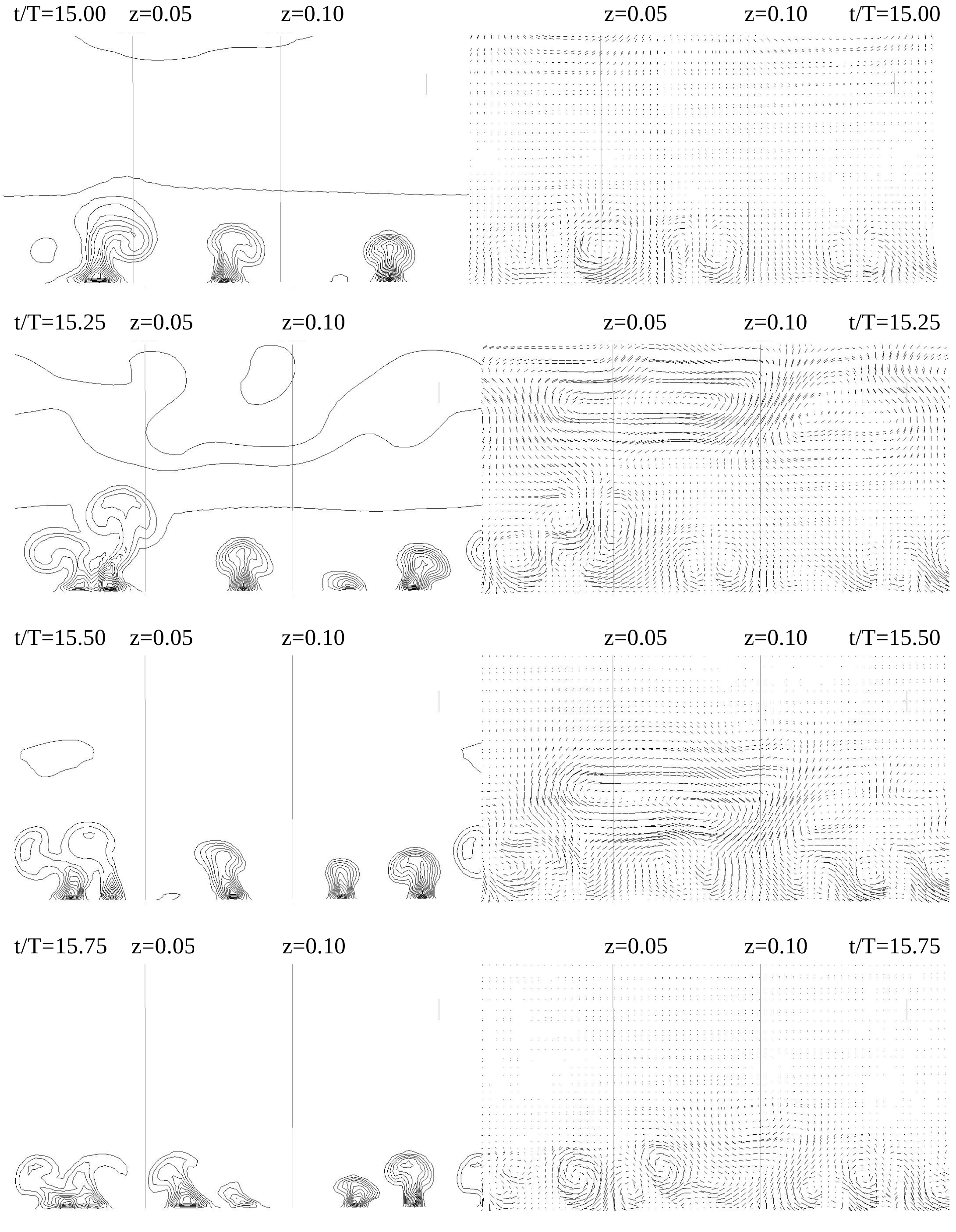

Figure 9. Plane perpendicular to the pressure surface at x/C_{ax}=0.7. Left: negative fluctuating streamwise velocity component (with respect to spanwise-averaged mean) (contour level from 0 to –0.3, step –0.015). Right: Fluctuating velocity vectors (spanwise-averaged mean subtracted).

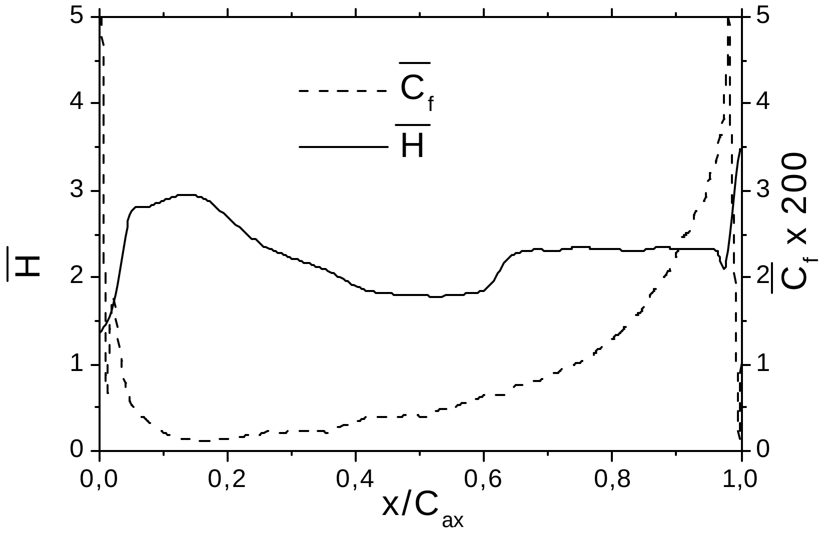

Figure 10. Time averaged $\overline{C_f}$, and $\overline{H}$, along the pressure side.

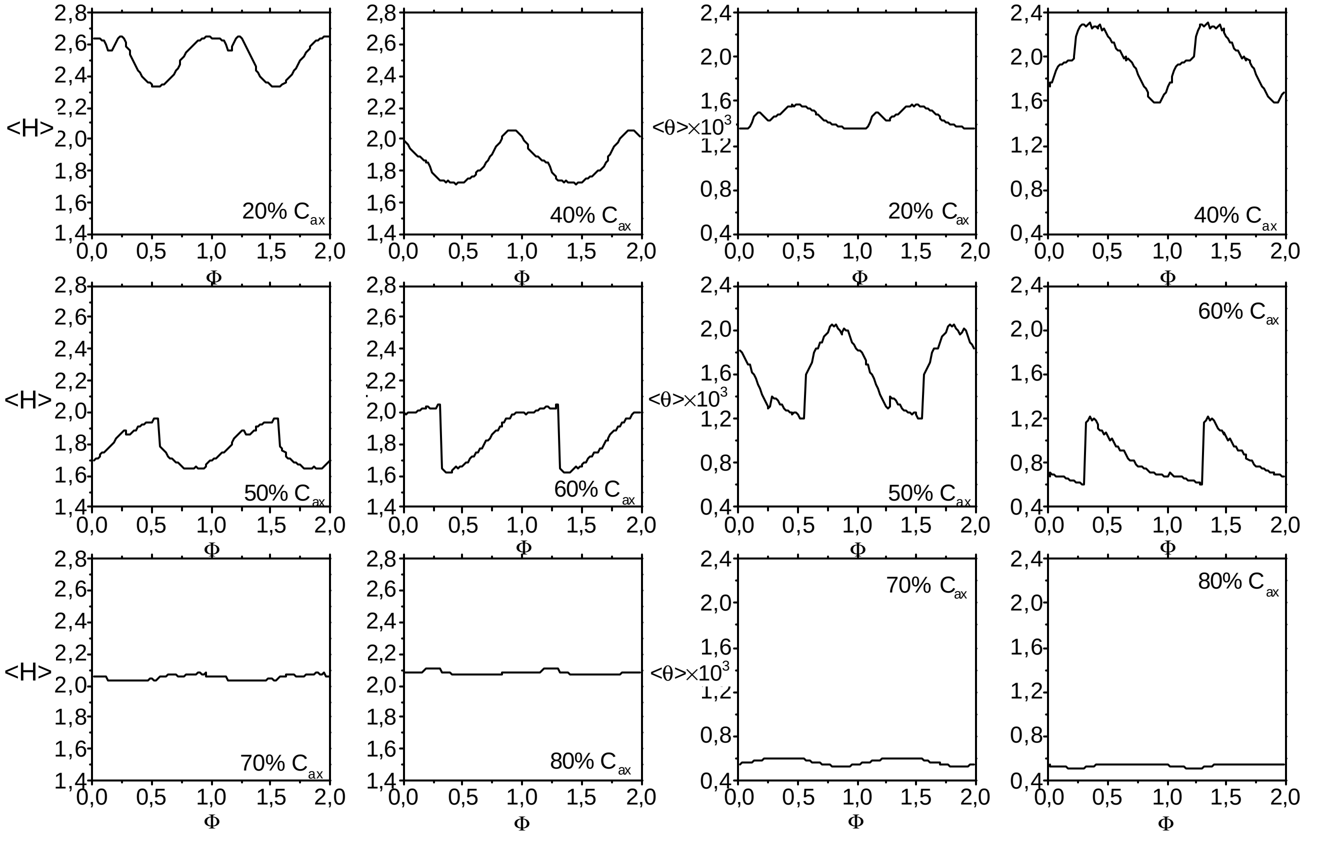

Figure 11. Phase averaged shape factor and momentum thickness at 20-40-50-60-70-80% C_{ax}.

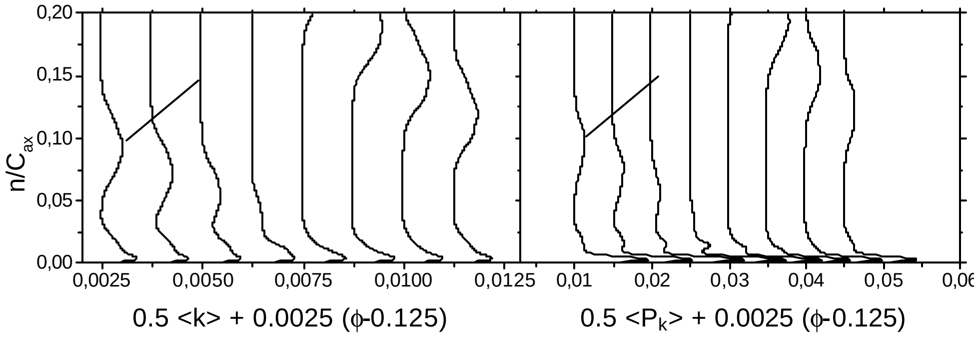

Figure 12. Turbulent kinetic energy (left) and production rate (right) at 60% C_{ax} for eight phase-averaged instants (plot shows eight curves for ϕ=0 to 0.875, step 0.125 from left to right).

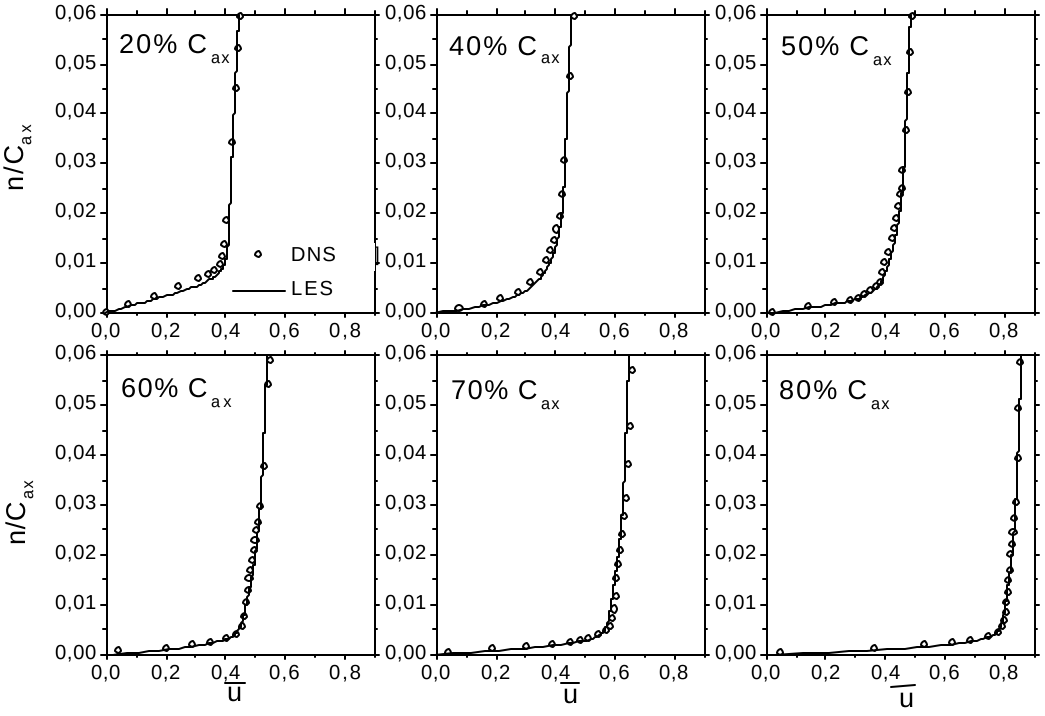

Figure 13. Profiles of time-averaged velocity at 20-40-50-60-70-80% C_{ax}:

solid lines = present LES; symbols = DNS [26].

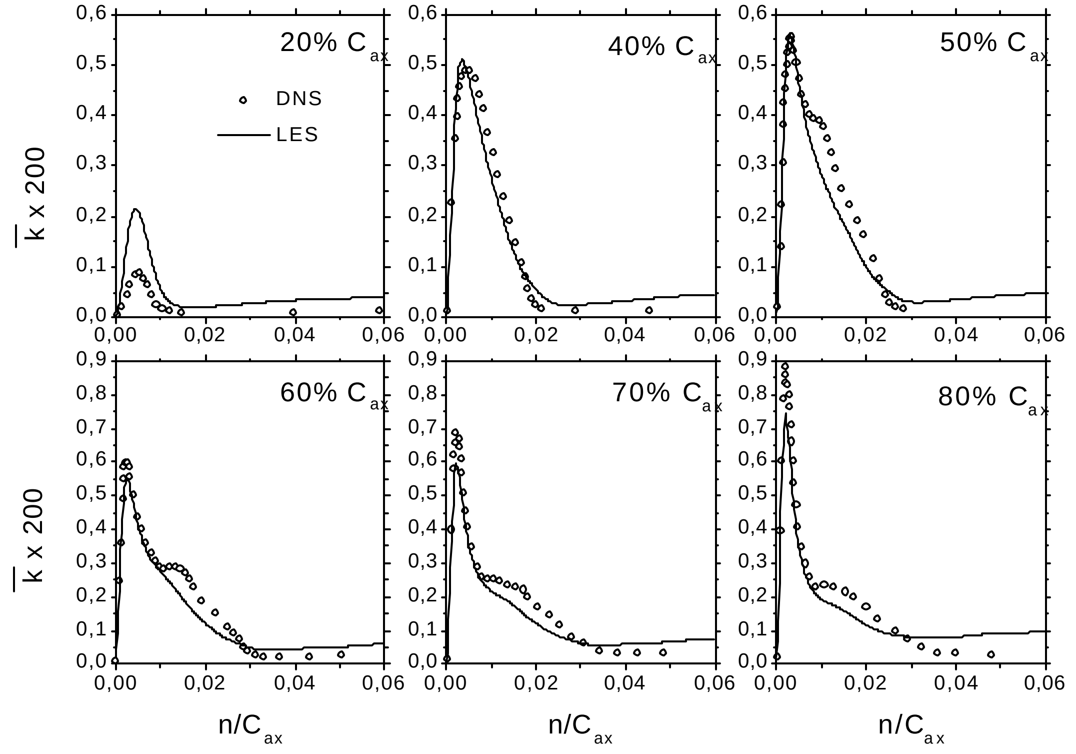

Figure 14. Profiles of time-averaged turbulent kinetic energy at 20-40-50-60-70-80% C_{ax}: solid lines = present LES; symbols = DNS [26]

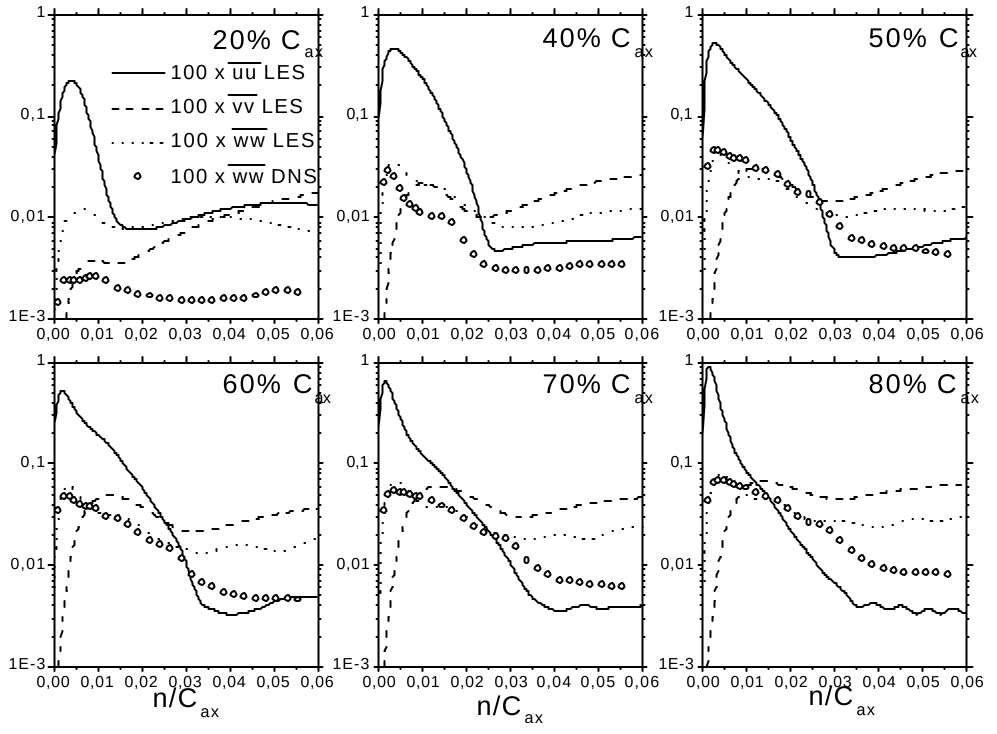

Figure 15. Profiles of normal stress components in the streamwise direction ($\overline{uu}$), in the blade-normal direction ($\overline{vv}$) and in the spanwise direction ($\overline{ww}$) at 20-40-50-60-70-80% C_{ax}: lines = present LES; symbols = DNS [26]

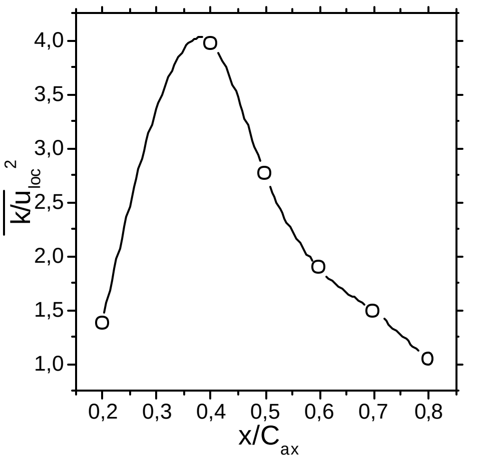

Figure 16. Turbulent kinetic energy peak made non-dimensional with respect to the peak velocity, u_{loc}, close to the pressure side wall.

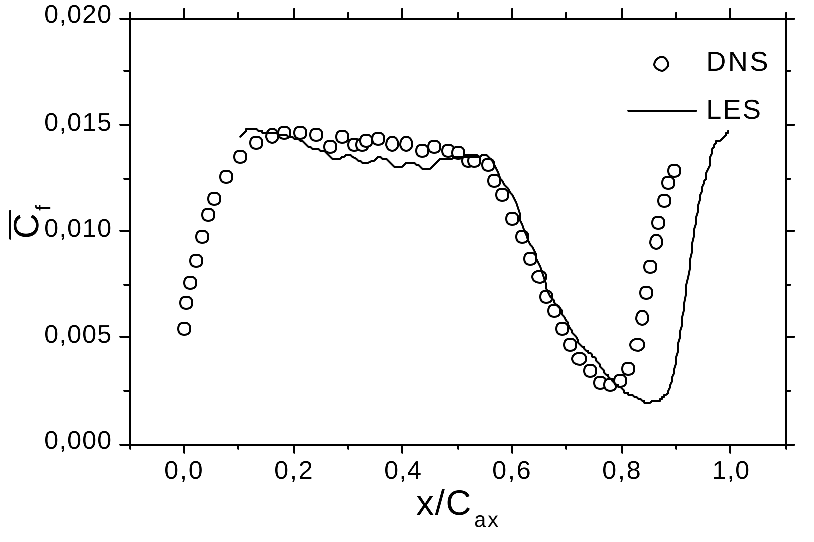

Figure 17. Time averaged $\overline{C_f}$ (×10) over the blade suction side.

DNS results are given in [26].

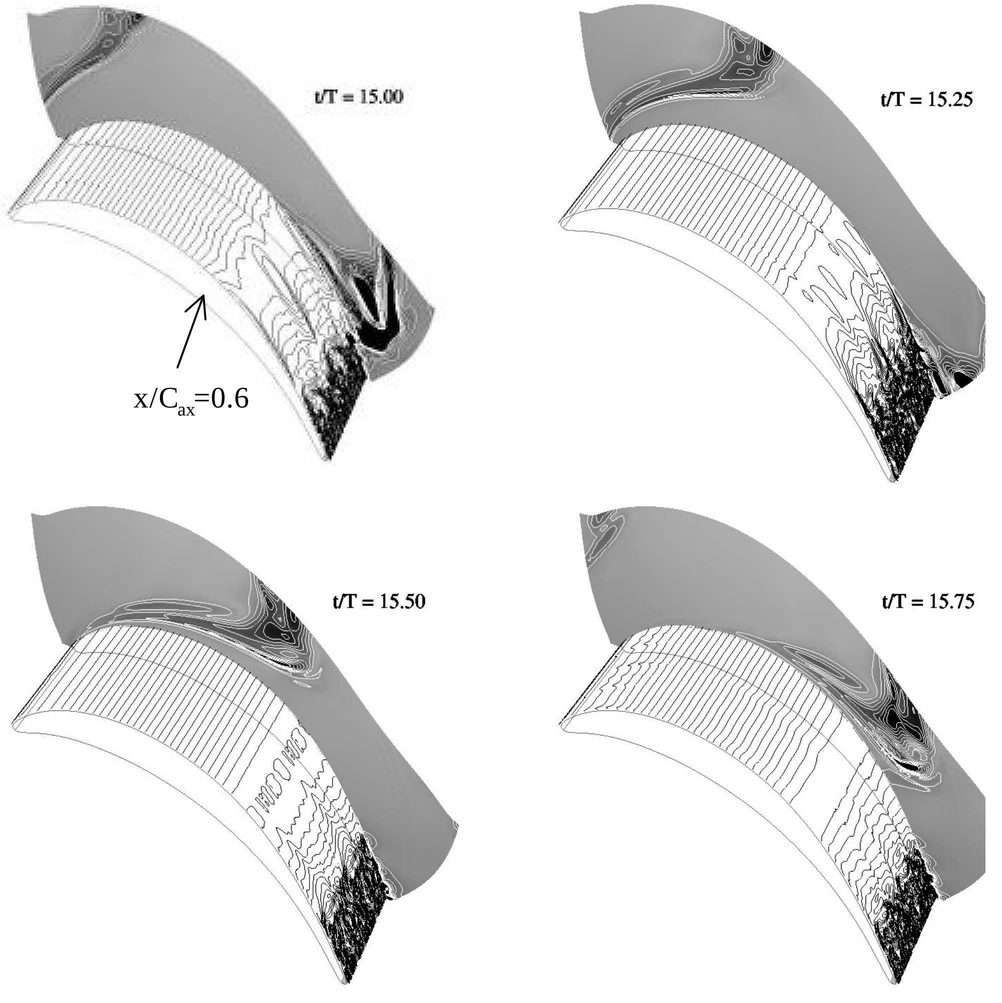

Figure 18. Isolines of the *v* velocity component over the suction side surface. The plots are generated on grid plane j=4 at a distance of about $0.002C_{ax}$ from the surface of the blade. The grey-scale on the back plane corresponds to the fluctuating velocity and is added to identify the location of wakes.

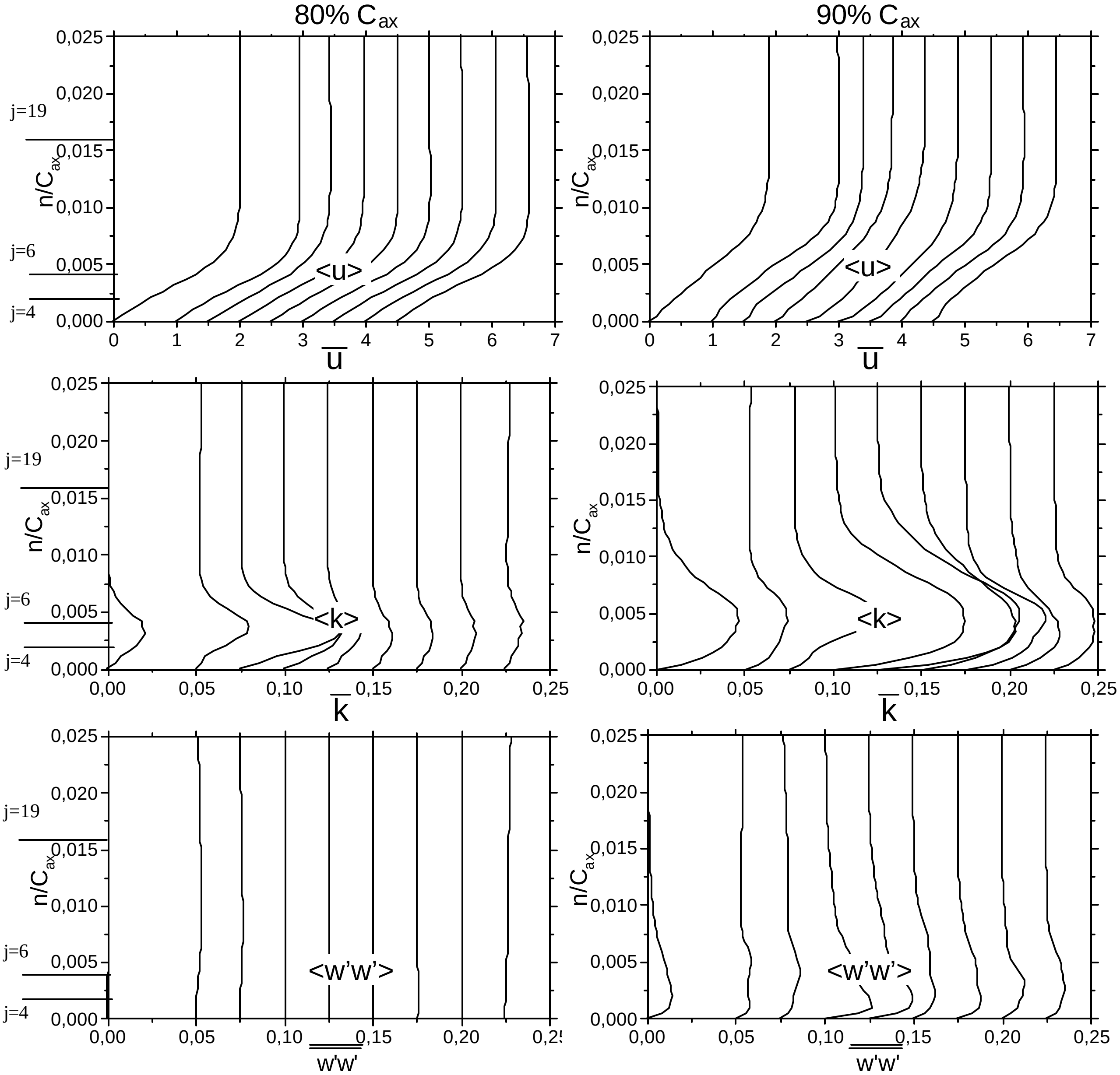

Figure 19. Profiles at x/C_{ax} = 0.8 (left) and x/C_{ax} = 0.9 (right) normal to the suction side of the blade of tangential velocity, fluctuating kinetic energy $\langle k \rangle$ and span-wise turbulent stress $\langle w'w' \rangle$. The profiles belong to the eight phase-averaged fields at Φ=0/8-7/8, the left-most profile is the time averaged one.

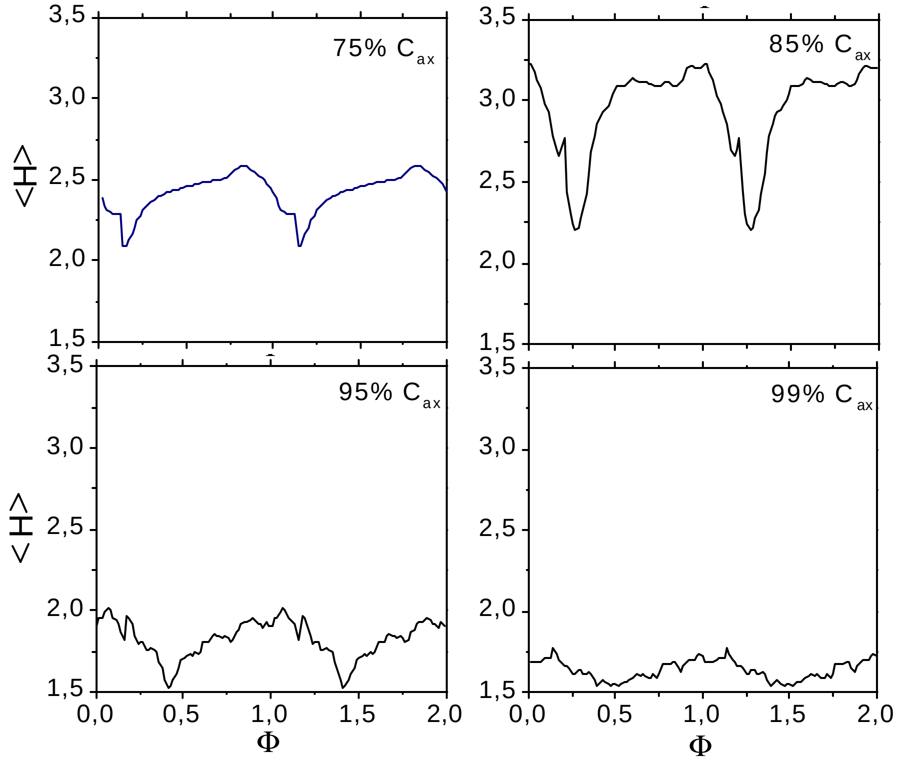

Figure 20. Phase-averaged shape factor ($\langle H \rangle$) for 4 sections normal to the suction side wall at x/C_{ax}=0.75-0.85-0.95-0.99.

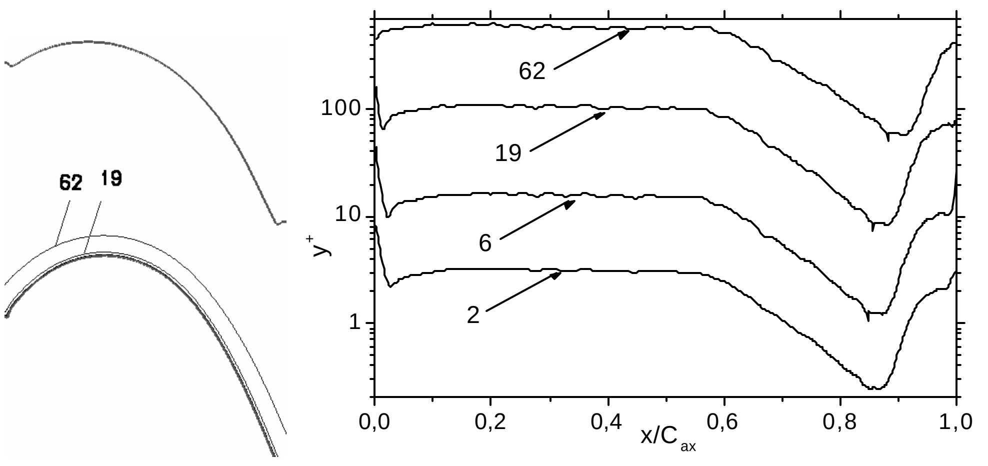

Figure 21. Selected monitor surfaces and their distance from the suction side of the blade in wall units.

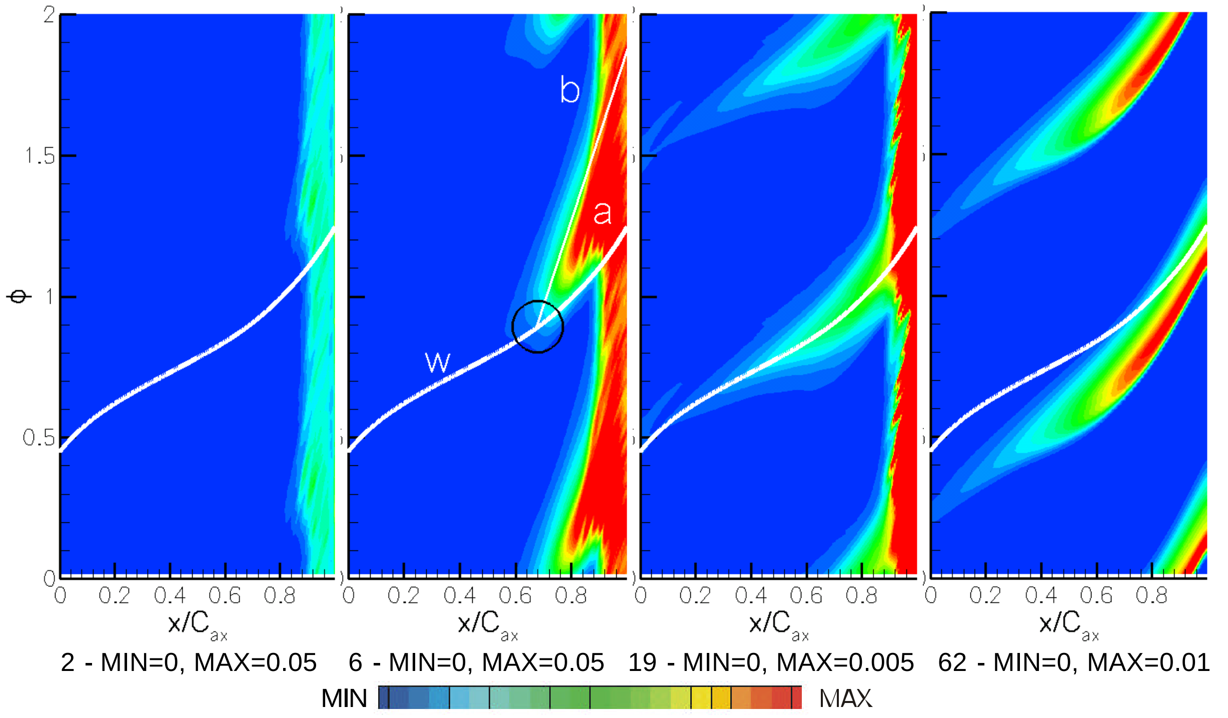

Figure 22. Space-time plots of the fluctuating kinetic energy along selected surfaces (x axis aligned with axial chord). The meaning of the white lines is detailed in the text.

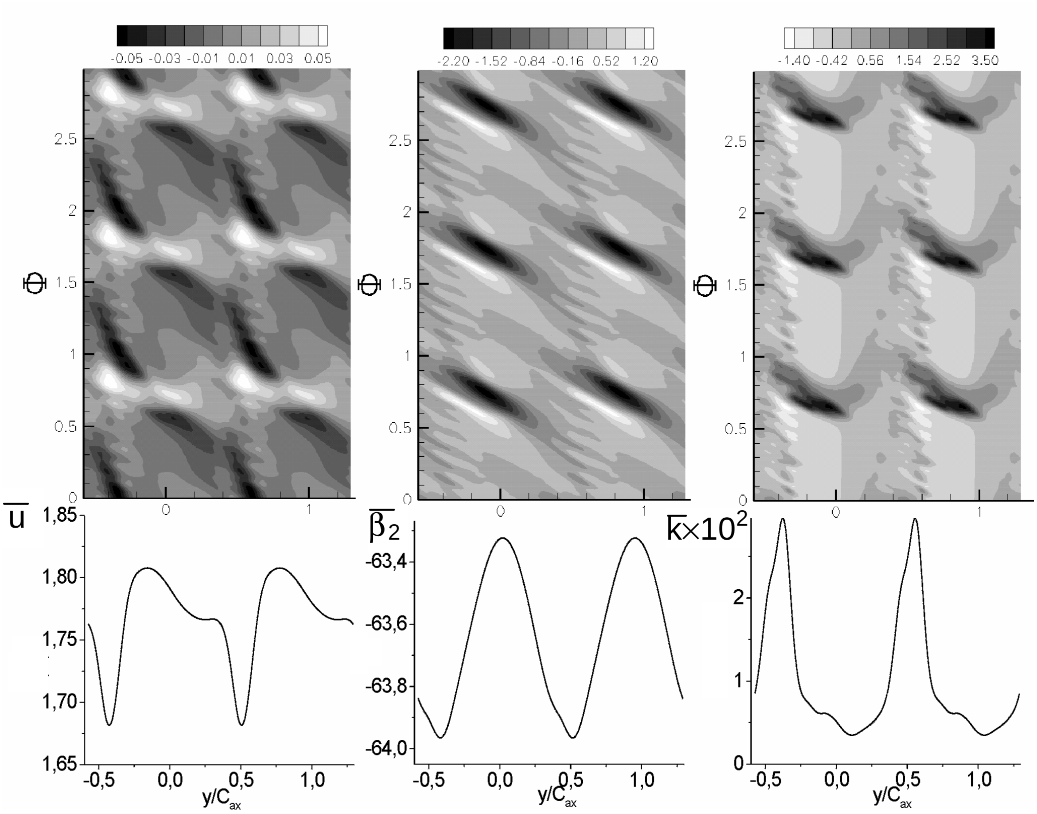

Figure 23. Space time plots and phase-averaged velocity magnitude, flow angle, and turbulent kinetic energy at x/C_{ax}=1.4.

Figure 24. Cascade geometry and grid used for LES (one out of 12 nodes is shown in both stream-wise and pitch-wise directions)

Figure 25. Distance between points in wall units at the blade suction side. Left: distance of wall-adjacent point to the surface, right: wall-parallel point-to-point distances.

Figure 26. Time-averaged static pressure distribution around the blade.

Figure 27. Principal axes of the time-averaged strain-rate tensor $\overline{S_{ij}}$, left (the thick vector identifies the direction of compression, the thin one that of stretching), and wake velocity $\langle \mathbf{v}_w \rangle = \langle \mathbf{v} \rangle - \overline{\mathbf{v}}$ at Φ=3/8, right (twin-thick parallel segments indicate the approximate width of the wake).

Figure 28. Phase-averaged velocity defect D at ϕ=0/8, 4/8, from left to right.

Figure 29. Instantaneous iso-surfaces of λ_2 in the blade vane for four selected times: t/T=14+0/8, 14+2/8, 14+4/8, 14+6/8 from top left clockwise.

Figure 30. Instantaneous iso-surfaces of λ_2 in proximity to the pressure side for four selected times t/T=14+0/8, 14+2/8, 14+4/8, 14+6/8 from top to bottom.

Figure 31. Fluctuating velocity vectors (spanwise-averaged mean subtracted) in the plane perpendicular to the pressure surface, x/C_{ax}=0.3, at eight consecutive instants t/T=15 to 16.75, step=0.25.

Figure 32. Plane perpendicular to the pressure surface at x/C_{ax}=0.7. Left: negative fluctuating streamwise velocity component (with respect to spanwise-averaged mean) (contour level from 0 to –0.3, step –0.015). Right: Fluctuating velocity vectors (spanwise-averaged mean subtracted).

Figure 33. Time averaged $\overline{C_f}$, and $\overline{H}$, along the pressure side.

Figure 34. Phase averaged shape factor and momentum thickness at 20-40-50-60-70-80% C_{ax}.

Figure 35. Turbulent kinetic energy (left) and production rate (right) at 60% C_{ax} for eight phase-averaged instants (plot shows eight curves for ϕ=0 to 0.875, step 0.125 from left to right).

Figure 36. Profiles of time-averaged velocity at 20-40-50-60-70-80% C_{ax}:
solid lines = present LES; symbols = DNS [26].

Figure 37. Profiles of time-averaged turbulent kinetic energy at 20-40-50-60-70-80% C_{ax}:
solid lines = present LES; symbols = DNS [26]

Figure 38. Profiles of normal stress components in the streamwise direction ($\overline{uu}$), in the blade-normal direction ($\overline{vv}$) and in the spanwise direction ($\overline{ww}$) at 20-40-50-60-70-80% C_{ax}:
lines = present LES; symbols = DNS [26]

Figure 39. Turbulent kinetic energy peak made non-dimensional with respect to the peak velocity, u_{loc}, close to the pressure side wall.

Figure 40. Time averaged $\overline{C_f}$ ($\times$10) over the blade suction side.
DNS results are given in [26].

Figure 41. Isolines of the *v* velocity component over the suction side surface. The plots are generated on grid plane j=4 at a distance of about $0.002C_{ax}$ from the surface of the blade. The grey-scale on the back plane corresponds to the fluctuating velocity and is added to identify the location of wakes.

Figure 42. Profiles at x/C_{ax} = 0.8 (left) and x/C_{ax} = 0.9 (right) normal to the suction side of the blade of tangential velocity, fluctuating kinetic energy $\langle k \rangle$ and span-wise turbulent stress $\langle w'w' \rangle$. The profiles belong to the eight phase-averaged fields at Φ=0/8-7/8, the left-most profile is the time averaged one.

Figure 43. Phase-averaged shape factor ($\langle H \rangle$) for 4 sections normal to the suction side wall at x/C_{ax}=0.75-0.85-0.95-0.99.

Figure 44. Selected monitor surfaces and their distance from the suction side of the blade in wall units.

Figure 45. Space-time plots of the fluctuating kinetic energy along selected surfaces (x axis aligned with axial chord). The meaning of the white lines is detailed in the text.

Figure 46. Space time plots and phase-averaged velocity magnitude, flow angle, and turbulent kinetic energy at x/C_{ax}=1.4.